Maastricht University

Multifaceted polymeric nerve guidance conduits with distinctive double-layered architecture and plasma-induced inner chemistry gradient for the repair of critical-sized defects

Citation for published version (APA):

Ghobeira, R., Wieringa, P., Van Vrekhem, S., Aliakbarshirazi, S., Narimisa, M., Onyshchenko, Y., De Geyter, N., Moroni, L., & Morent, R. (2022). Multifaceted polymeric nerve guidance conduits with distinctive double-layered architecture and plasma-induced inner chemistry gradient for the repair of critical-sized defects. *Biomaterials Advances*, *143*, Article 213183. https://doi.org/10.1016/j.bioadv.2022.213183

Document status and date:
Published: 01/12/2022

DOI:
10.1016/j.bioadv.2022.213183

Document Version:
Publisher's PDF, also known as Version of record

Document license:
Taverne

Please check the document version of this publication:

- A submitted manuscript is the version of the article upon submission and before peer-review. There can be important differences between the submitted version and the official published version of record. People interested in the research are advised to contact the author for the final version of the publication, or visit the DOI to the publisher's website.
- The final author version and the galley proof are versions of the publication after peer review.
- The final published version features the final layout of the paper including the volume, issue and page numbers.

Link to publication

General rights
Copyright and moral rights for the publications made accessible in the public portal are retained by the authors and/or other copyright owners and it is a condition of accessing publications that users recognise and abide by the legal requirements associated with these rights.

- Users may download and print one copy of any publication from the public portal for the purpose of private study or research.
- You may not further distribute the material or use it for any profit-making activity or commercial gain
- You may freely distribute the URL identifying the publication in the public portal.

If the publication is distributed under the terms of Article 25fa of the Dutch Copyright Act, indicated by the “Taverne” license above, please follow below link for the End User Agreement:

www.umlib.nl/taverne-license

Take down policy
If you believe that this document breaches copyright please contact us at:

repository@maastrichtuniversity.nl

providing details and we will investigate your claim.

Download date: 25 Apr. 2024

143 (2022) 213183

Contents lists available at ScienceDirect

Biomaterials Advances

journal homepage: www.journals.elsevier.com/materials-science-and-engineering-c

Multifaceted polymeric nerve guidance conduits with distinctive double-layered architecture and plasma-induced inner chemistry gradient for the repair of critical-sized defects

Rouba Ghobeira [a,*], Paul Wieringa [b], Stijn Van Vrekhem [a], Sheida Aliakbarshirazi [a], Mehrnoush Narimisa [a], Yuliia Onyshchenko [a], Nathalie De Geyter [a], Lorenzo Moroni [b], Rino Morent [a]

[a] Research Unit Plasma Technology (RUPT), Department of Applied Physics, Faculty of Engineering and Architecture, Ghent University, Sint-Pietersnieuwstraat 41 B4, 9000 Ghent, Belgium
[b] Department of Complex Tissue Regeneration, MERLN Institute for Technology-Inspired Regenerative Medicine, Maastricht University, Universiteitsingel 40, 6229ER, Maastricht, the Netherlands

ARTICLE INFO

Keywords:
Nerve guidance conduits
Electrospinning
Nanofibers
Tissue engineering
Polyactive®
Plasma treatment
Schwann cells
Cell chemotaxis

ABSTRACT

Despite tissue engineering advances, current nerve guidance conduits (NGCs) are still failing in repairing critical-sized defects. This study aims, therefore, at tackling large nerve gaps (2 cm) by designing NGCs possessing refined physicochemical properties enhancing the activity of Schwann cells (SCs) that support nerve regeneration over long distances. As such, a combinatorial strategy adopting novel plasma-induced surface chemistry and architectural heterogeneity was considered. A mechanically suitable copolymer (Polyactive®) was electrospun to produce nanofibrous NGCs mimicking the extracellular matrix. An innovative seamless double-layered architecture consisting of an inner wall comprised of bundles of aligned fibers with intercalated random fibers and an outer wall fully composed of random fibers was conceived to synergistically provide cell guidance cues and sufficient nutrient inflow. NGCs were subjected to argon plasma treatments using a dielectric barrier discharge (DBD) and a plasma jet (PJ). Surface chemical changes were examined by advanced X-ray photoelectron spectroscopy (XPS) micro-mappings. The DBD homogeneously increased the surface oxygen content from 17 % to 28 % on the inner wall. The PJ created a gradient chemistry throughout the inner wall with an oxygen content gradually increasing from 21 % to 30 %. In vitro studies revealed enhanced primary SC adhesion, elongation and proliferation on plasma-treated NGCs. A cell gradient was observed on the PJ-treated NGCs thus underlining the favorable oxygen gradient in promoting cell chemotaxis. A gradual change from circular to highly elongated SC morphologies mimicking the bands of Büngner was visualized along the gradient. Overall, plasma-treated NGCs are promising candidates paving the way towards critical nerve gap repair.

1. Introduction

Despite all neurology advancements, severe peripheral nerve injuries remain a major clinical challenge [1]. In fact, nerve gap defects accompanied with tissue loss are precluded from the direct repair because of the unwanted tension that the nerve ends undergo during fascicular coaptation [2]. The interposition of a supportive structure spanning the injury site becomes therefore unavoidable in most transection defects. In the past 50 years, nerve autografts have been considered the gold standard to bridge peripheral nerve damages. This supremacy is however deprecated by several drawbacks, such as the use of sensory-only donor nerves, morphometric fascicular mismatching and possible scarring and neuroma formation, which confine the success rate to only 50 % [3–5]. As an alternative, tissue engineers have adopted the entubulation approach by firstly designing hollow nerve guidance conduits (NGCs) typically consisting of a physical scaffolding made up of polymeric material [1]. Nonetheless, nerve regeneration inside such constructs has been very limited or even completely absent in gaps exceeding 1 cm [6,7]. Extra cell-supportive cues have also been implemented including: 1) structural cues (e.g. addition of intra-luminal

---

* Corresponding author.
E-mail address: Rouba.Ghobeira@ugent.be (R. Ghobeira).

https://doi.org/10.1016/j.bioadv.2022.213183
Received 16 June 2022; Received in revised form 30 October 2022; Accepted 1 November 2022

fillers, creation of a nanofibrous wall, fabrication of multi-channel NGCs…), 2) mechanical cues (e.g. use of different tailorable synthetic polymers as base material) and 3) molecular cues (e.g. administration of neurotrophic factors…). Despite triggering more promising outcomes, these advanced NGCs still fail in outperforming or even matching the morphometric and functional regeneration levels of the autograft especially in critical nerve gaps (≥1.5 cm) [4,8]. Therefore, the goal of this paper is to tackle large nerve gaps (2 cm) by adopting a combinatorial strategy merging the advantages of previous NGCs and implementing additional innovative levels of complexity involving interfaces, chemical gradients and architectural heterogeneity. As such, designing a novel NGC possessing ideal structural, mechanical and biochemical properties boosting the activity of Schwann cells (SCs), being the main glial cells governing the intrinsic regeneration of mature nerves over long distances, is aimed at [9]. In fact, SCs play a vital role in governing axonal regrowth via their: 1) migration from both ends of the injured nerve, proliferation and orientation into longitudinal bands known as bands of Büngner that act as a guiding path for regenerating axons; 2) secretion of neurotrophic factors and extracellular matrix (ECM) molecules such as collagen and laminin; 3) expression of nerve cell adhesion molecules and receptors which makes them a favored substrate for axon attachment and migration and 4) assistance in an advanced stage of the regenerative sequence in the remyelination of the regenerated axons [9,10]. However, when the nerve gap reaches a critical length, SC migration from both nerve ends and proliferation decline and SC numbers become insufficient to create a conductive environment [11]. Therefore, seeding SCs on NGCs pre-implantation started to be considered as gold standard cellular-based approaches in nerve repair. In fact, Xie et al. have shown that polycaprolactone (PCL) NGCs pre-seeded with SCs enhanced nerve fiber sprouting and motor recovery post-implantation in a rat sciatic nerve gap (14 mm) compared to their SC-free counterparts [2]. Similarly, fibrin-SC NGCs exhibited an increased rate of axonal regeneration across a 10 mm nerve defect compared to acellular NGCs [12]. Nonetheless, in order to further enhance the regeneration-promoting ability of SCs in critical defects, proper structural guidance support is needed [7,9,10].

One structural-based strategy that was previously adopted to direct nerve growth and promote SC migration over long distances took the form of NGCs with intra-luminal fillers. However, the addition of such fillers was shown to face challenging considerations such as the high “packing density” inhibiting the regeneration or the “void fraction” leading to the settlement of the fillers at the NGC bottom [8]. Multi-channel NGCs were also designed given their mimicry of the nerve micro-architecture but were associated with the risk of channels occlusion after polymer swelling thus blocking axon regrowth [13]. NGCs made up of nanofibers have shown moderate successes over the other investigated configurations given their mimicry of the neural ECM governing vital cellular functions [3]. Particularly, aligned nanofibers were proven to be good candidates in nerve tissue engineering as they provide cell guidance contact promoting directed neurite extension and SC elongation and migration [5,14,15]. Nonetheless, the parallel arrangement and high packing density of aligned fibers hamper the inter-fiber porosity thus cutting off the crucial nutrient supply to the NGC lumen [16]. Moreover, an NGC wall fully composed of aligned fibers is predisposed to tearing along the fiber direction after the frequent suture piercings of the surgical implantation [2]. In order to circumvent these challenges, double-layered NGCs with inner aligned and outer random fibers were conceived in few previous studies. However, the conduit fabrication was mostly done in a complicated multi-step process implicating a separate electrospinning of random and aligned fibrous membranes that are stacked on top of each other, rolled up to form a tube and secured using glue, solvents or heating [2,15,17]. In addition, this fabrication strategy gives a non-uniform NGC engendering mechanical weaknesses and discontinuities associated with the presence of seams in the NGC wall. Moreover, the outer layer and the luminal layer that still lacks pores might disconnect and the risk of conduit opening in vivo becomes high [5,14].

Next to the importance of the topographical cues, a meticulous selection of a base material exhibiting mechanical properties closely matching those of the soft nerve tissue while resisting external stretching forces and retaining a steady shape during the regenerative sequence is crucial. The potential collapse of the NGCs in vivo can actually constitute a serious burden as it can compress the regenerating nerve or completely block its regeneration [18]. Based on the results of a recent study in which the copolymer poly(ethylene oxide terephthalate)-poly (butylene terephthalate) (PEOT-PBT) commercially known as Polyactive® (PA) was used for the first time to fabricate NGCs, this copolymer was chosen to be the base NGC material in this study. In addition to its biocompatibility and easy processability, the first advantage of PA over conventional polymers is the possibility to exclusively tailor the material properties by controlling its composition [4]. A selected ratio of 55/45 PEOT/PBT was previously shown to generate electrospun NGCs having an ultimate tensile strength (2.6 MPa) closely matching the one of a rat sciatic nerve (2.7 MPa as was assessed by Borschel et al.) and a higher elasticity (Young's modulus: 10.5 MPa) than NGCs made of conventional synthetic and natural polymers like PCL and chitosan [19,20]. These mechanical properties were revealed to support nerve regeneration in vivo. Additionally, despite their relatively thin wall and the high degree of porosity, PA conduits did not collapse and remained intact four months after implantation [4].

A critical limitation of most synthetic and mechanically tailorable NGCs is their deprivation of immobilized proteins because of their hydrophobic base material lacking polar functional groups. Both topographical and biochemical cues are concurrently recognized by cells at the cell-scaffold interface and play an essential role in the initiation of cellular processes such as adhesion and proliferation [21,22]. However, given the narrow dimensions of the porous conduits, reaching and modifying the inner wall surface without altering the nanofibers delicate structure remain challenging tasks. As such, free neurotrophic factors have been added to NGCs for their known ability to promote axon growth but were shown to have no effect because of their leakage, inactivation, inadequate delivery method or even adverse effects due to unexpected activation of unwanted signaling pathways [3,23]. To solve this issue and essentially support SCs-NGC adhesion, this study focuses on the application of non-thermal plasmas as a route to bio-activate the NGC's surface. Plasma treatment is nowadays gaining a great interest over other surface modification techniques due to its solvent-free, simplicity, gas-based and highly controllable aspects enabling the incorporating of specific functional groups on the surface of complex porous scaffolds, hence NGCs. More importantly, plasma treatment is distinguished by its non-invasive character limited to a modification depth of few nanometers thus preserving the topography and bulk mechanical properties of subtle nanofibrous scaffolds [21,24–26]. Despite the considerable improvements offered by plasma-functionalized scaffolds in several tissue engineering applications, plasma treatment was never applied, to the best of our knowledge, to electropsun NGCs. Very few researchers have fabricated NGCs by again rolling up polymeric micropatterned films pre-subjected to a plasma treatment and coated these with biomolecules such as laminin [27–30]. Nevertheless, no surface chemical characterization was performed post-plasma treatment thus hampering biomolecule immobilization as a result of non-optimized process conditions. Moreover, next to the high cost of biomolecules, their immobilization might lead to a reduced biological activity caused by some conformational changes. In fact, the incorporation of oxygen-containing functionalities on nanofiber meshes was proven to enhance cellular activities via a controlled and spontaneous adsorption of proteins post-immersion in the cell media [31]. For instance, Prabhakaran et al. observed an improved SC adhesion on air plasma-treated PCL fibers compared to untreated fibers but also to PCL/collagen fibers, thus underlining the absolute importance of plasma-induced oxygen functionalities [32].

In the body, the directional regeneration of axons over long distances is mediated by growth cone chemotaxis following spatial gradients of neuro-stimulatory molecules [33]. Few authors have successively filled the NGCs with hydrogels containing different concentrations of nerve growth factor loaded into nanoparticles or microtubules thus conceiving a biomolecular gradient [8,34,35]. In addition to the complexity of this approach, the hydrogels isotropic nature lacks topographical cues and thus the necessary microstructure aligning the cells. Wet chemistry approaches were also used to immobilize growth factors in a gradient way on NGCs by a differential exposure to solutions with varying concentrations and/or reaction times along NGCs [5,8,33]. Nonetheless, such treatments can damage the fine nanofibrous structure of electrospun NGCs, alter their mechanical performance and increase their degradation rate. Moreover, the focus of such studies was solely directed towards the extension and elongation of axons. However, the extent of directional migration of SCs into the defect gap, which was overlooked in the design of NGCs, is the underlying key dictating the axonal regeneration in vivo[36]. After migration, SCs proliferate and align to form the so-called bands of Büngner structure supporting and guiding nerve regeneration [9,37]. Recently, few authors have studied SC migration on micro-gradient surfaces engineered by immobilizing polymer brushes and/or peptides on glass substrates using complex wet chemical treatments prone to damage nanofibers [36,38].

In view of these challenges, the present study proposes a simple one-step electrospinning of novel bi-layered PA NGCs with an inner wall

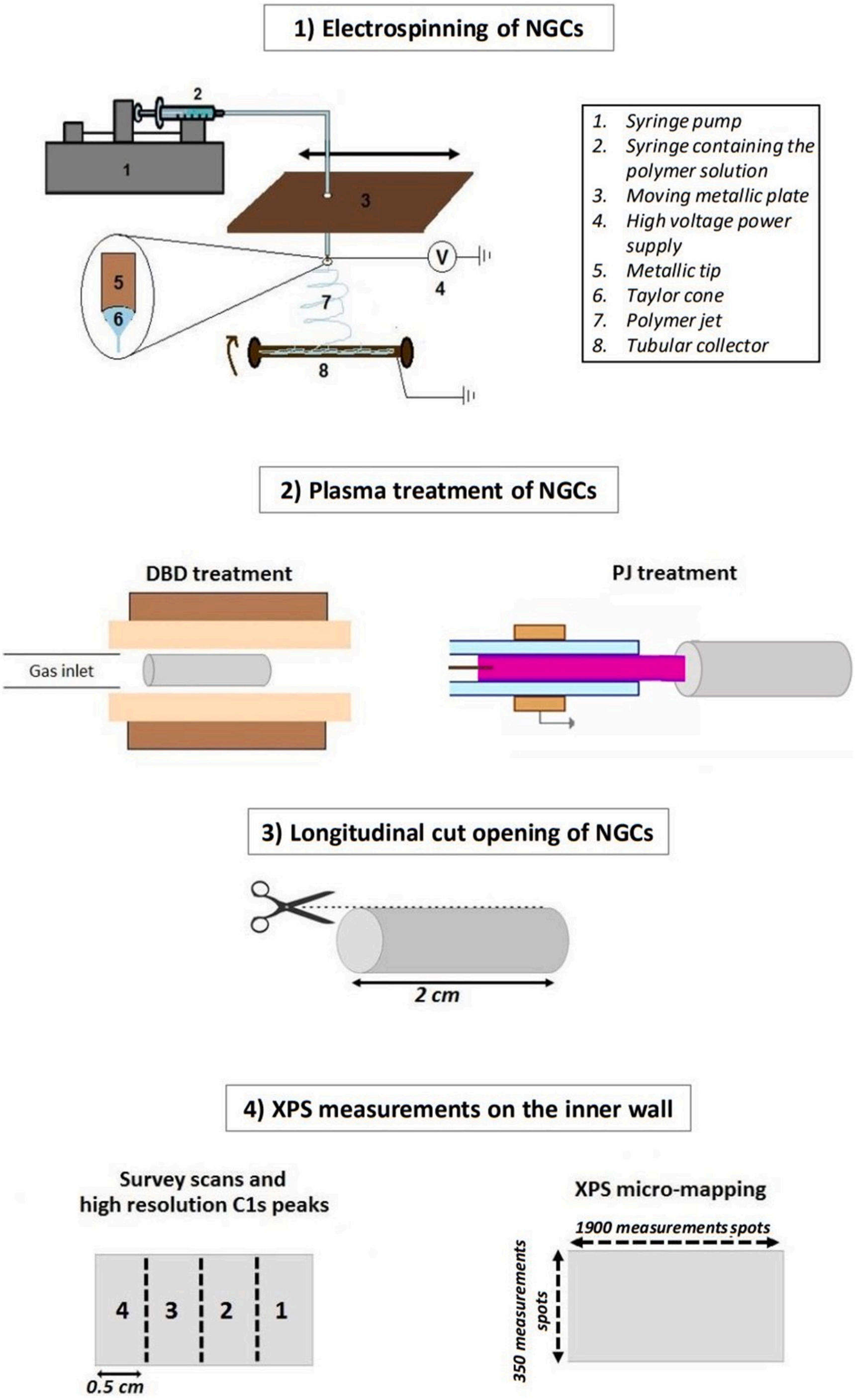

Fig. 1. Schematic illustrations of the steps followed to electropun, plasma-treat and perform XPS measurements on NGCs.

composed of bundles of aligned fibers intercalated between random fibers and an outer wall completely composed of random fibers. Thereafter, a dielectric barrier discharge (DBD) and a simple plasma jet (PJ) are used to functionalize the NGC inner wall in homogeneous and gradient ways along its length respectively. To the best of our knowledge, no study has reported so far the formation of a surface chemistry gradient inside NGCs without the use of any growth factor. This approach is believed to induce the directional path-finding ability of axons but also the chemotaxis of SCs towards the distal target. The surface chemistry is then characterized by means of advanced X-ray photoelectron spectroscopy (XPS) measurements including exclusive micro-mappings visualizing with very high precision (resolution of 10 μm) the exact distribution of plasma-induced oxygen over the inner wall (Fig. 1). The morphology, surface roughness, swelling index, surface wettability and mechanical properties of the NGCs pre- and post-plasma treatments are then evaluated. A comparative in vitro study is then performed to assess the behavior of SCs seeded on untreated and plasma-treated NGCs with homogeneous and gradient surface chemistries. Finally, in order to predict the efficiency of the SC-seeded NGCs in boosting neurite extension from the proximal end and as such enhancing nerve regeneration in critical defects, a co-culture with neuron-like pheochromocytoma (PC12) cells is carried out. This cell type is purposely chosen giving its well-known capacity of neural differentiation and neurite extension in adequate environments, thus establishing an ideal model for a first proof-of-concept study.

2. Materials and methods

2.1. NGC base material

PA was provided by PolyVation B.V. (Groningen, The Netherlands) in the form of 300PEOT55PBT45 that follows the annotation aPEOTbPBTc where a is the molecular weight (in g/mol) of the base polyethylene glycol (PEG) segments used during polymerization while b and c represent the weight ratio between PEOT and PBT respectively. Prior to electrospinning, the copolymer was dissolved overnight in the solvent system chloroform ($CHCl_3$, Sigma-Aldrich-The Netherlands)/ 1,1,1,3,3,3-hexafluoro-2-propanol (Bisolve, The Netherlands) at a ratio of 7:3 *v*/v to obtain a polymer concentration of 25 % (*w*/*v*).

2.2. Electrospinning

NGCs were biofabricated using a custom-made electrospinning apparatus maintaining the temperature at 25 °C and the relative humidity at 30 % for a sustained reproducibility. The device was designed in a way allowing the jet to be sprayed in a descending track towards a rotating tubular collector (diameter: 2 mm, length: 30 mm) connected to the ground. A distance of 13.5 cm was fixed between the collector and the spinneret being a blunt 20-gauge hypodermic needle made of stainless steel (diameter: 0.8 mm, Unimed, Switzerland). This needle was mounted on a charged metallic plate and programmed to translate in a back and forth motion along the collector axis (120 mm/min) for a homogeneous fiber deposition over the NGC length. A schematic representation of the device is illustrated in Fig. 1.1. During the electrospinning process, the polymer solution, loaded in a syringe, was continually pushed by means of a KD scientific syringe pump at a constant flow rate of 1 ml/h to reach the spinneret. By applying a voltage of 20 kV through a DC high voltage supply (Gamma High Voltage Research, USA), nanofibers could be collected on the tubular collector thus forming conduits. An even wall thickness was safeguarded by rotating the mandrel at a speed of 50 rpm. After electrospinning for 10 min, the collector was detached and placed in 70 % ethanol for an easy removal of the NGCs that were then left to dry in ambient air. All NGCs were then made equal in length (2 cm) by cutting off 5 mm of each extremity.

2.3. Plasma surface functionalization

2.3.1. DBD treatment

After electrospinning, PA NGCs were subjected to a medium pressure air or Ar plasma treatment by placing them horizontally in between the 2 parallel plates of an in-house designed DBD reactor that was entirely described and electrically characterized in previous papers [26,39] (Fig. 1.2). In short, the reactor consisted of 2 major components: an AC power supply and a cylindrical plasma chamber encompassing 2 circular copper plates (diameter: 4 cm) covered each by a ceramic dielectric (Al_2O_3, thickness: 0.7 mm). The lower copper plate acting as a grounded electrode was coupled to earth through a 10.4 nF capacitor or a 50 Ω resistor while the upper plate corresponding to the high-voltage electrode was connected to the power source (frequency: 50 kHz). The gap between both electrodes was fixed at 4 mm and fed by a unidirectional horizontal gas flow regulated by means of an El-Flow system (Bronkhorst®, The Netherlands). A rotary vane pump was connected to the plasma chamber in order to evacuate it and subsequently infuse it with a reproducible atmosphere.

In a pre-plasma preparative step, the discharge chamber containing the sample was pumped down to reach a pressure of at least 0.6 kPa. Thereafter, the reactor was pervaded with air or Ar (Alphagaz 1 - Air Liquide, Belgium) at a flow rate of 3 slm (standard liters per minute). The pressure was regulated and fixed at 90 kPa for 3 min to establish a homogeneously distributed gas composition throughout the chamber. The actual plasma treatment was then carried out at a gas flow rate of 1 slm, a sub-atmospheric pressure of 5 kPa and a power of 1.5 W for both air and Ar discharges to enable an accurate comparison. Based on recorded current-voltage waveforms, it was revealed that the air and Ar discharges operated in filamentary and glow modes respectively.

2.3.2. PJ treatment

Next to the DBD treatments, a direct plasma penetration inside the NGCs was performed using an atmospheric pressure PJ operating in Ar. A detailed description, representation and electrical characterization of the set-up can be found in a previous work [40] (Fig. 1.2). In brief, it consisted of a quartz capillary containing a needle electrode and encircled on the outside by a ring-shaped electrode. The capillary had an outer and inner diameter of 3 mm and 1.3 mm respectively. The needle electrode that was connected to an AC high voltage source was made up of a tungsten wire having a diameter of 0.5 mm with a half sphere-shaped tip. The ring-shaped grounded electrode was 10 mm long, made of copper and located at a distance of 35 mm from the needle electrode. The distance between the copper ring center and the capillary edge was fixed at 20 mm. An Ar flow running inside the capillary was regulated by a Bronckhorst El-Flow controller at a rate of 1 slm. When applying a high voltage to the tungsten electrode, plasma appeared in the inter-electrode gap and outflew from the capillary to propagate in the surrounding air, formed the so-called effluent plasma and penetrated in the NGCs placed at a distance of 5 mm from the capillary edge. This plasma jet was produced at a fixed frequency of 60 kHz, a peak-to-peak amplitude of 7 kV and a discharge power of 3 W.

2.4. Surface characterization

2.4.1. XPS analysis

In order to determine the surface chemical composition of the untreated and plasma-treated NGCs, XPS measurements were carried out by means of a PHI 5000 Versaprobe II spectrometer. Since the main interest resided in the chemistry of the inner wall, the NGCs were longitudinally cut open (Fig. 1.3). The luminal surface was then excited, over a squared area of 500 × 500 μm^2, with an X-ray beam size of 100 μm originating form a monochromatic Al K_α X-ray source ($h\nu = 1486.6$ eV) running at a power of 50 W. The resultant photoelectrons emitted from the NGC surface were detected by a hemispherical analyzer placed at an inclination of 45° with respect to the normal of the luminal surface.

All along the measuring process, the main specimen chamber was constantly maintained at a pressure of at least 10^{-6} Pa. Survey scans and C1s high-resolution peaks were recorded on 4 different zones (0.5 cm each) of the NGCs with pass energies of 187.85 eV and 23.5 eV and step sizes of 0.1 eV and 0.8 eV respectively. The different zones were numbered based on the position of the conduits in the DBD and the PJ: zone 1 and zone 4 being respectively the farthest and the closest from the DBD gas inlet or the PJ capillary end (Fig. 1.4). The identification and quantification of the present surface elements were done by analyzing the survey scans through Multipak software (V 9.6) employing a Shirley background and complying with the relative sensitivity factors assigned by the device's manufacturer. The binding energy scale was calibrated with respect to the hydrocarbon peak of the C1s spectrum being at 285.0 eV. The same software was also used to determine the chemical bonds via a deconvolution of the C1s spectra. To do so, a curve fitting was carried out using Gaussian-Lorentzian peaks (80–100 %) with full width at half maximum (FWHM) confined below 1.5 eV. All XPS values reported in the paper represent the average of 4 measurements taken on 2 different samples of the same conditions.

XPS micro-mapping was also performed on the plasma-treated NGCs to study, with a distinctively high precision, the exact distribution of oxygen and carbon over the complete inner wall surface. A matrix of 38 × 7 spots selected at 10 μm intervals vertically and horizontally was created in way accurately covering the inner NGC wall. This was done by a scanning X-ray induced (SXI) secondary electron image camera connected to the XPS device and allowing a precise navigation over the sample surface. A chemical mapping involving individual high resolution C1s and O1s spectra recorded with a step size of 0.4 eV and a pass energy of 93.9 eV was then performed in an unscanned mode with a spatial resolution of 10 μm. In fact, each measurement spot (= 500 μm^2) was divided into analysis areas of 10 μm^2 giving a map of 50 × 50 pixels (2500 values). After analyzing each map separately using Multipak software (V 9.6), all individual maps were stitched together thus generating an oxygen map of 1900 × 350 pixels on the inner NGC surface (Fig. 1.4).

2.4.2. WCA analysis

The surface wettability of the inner NGC wall was assessed before and after the different plasma treatments by means of water contact angle (WCA) measurements using a Krüss Easy Drop optical system (Krüss Gmbh, Germany). To do so, the NGCs were cut opened, then distilled water droplets of 2 μL were deposited on the inner surface using an automated high-precision liquid dispenser. The WCAs were then measured by means of Laplace-Young curve fitting. The reported values are presented as mean WCA values ± standard deviation after averaging out 6 values measured on 3 different NGCs for every condition.

2.4.3. SEM analysis

The nanofibers forming the inner and outer walls of the NGCs were visualized using the JSM-6010PLUS (JEOL, Japan) scanning electron microscope (SEM). To do so, the NGCs were firstly cut open and coated on their inner or outer surface with a thin layer of fine gold particles by means of a JFC-130 autofine coater (JEOL, Japan). Thereafter, the actual SEM images were acquired at an accelerating voltage of 7 kV. ImageJ (National Institutes of Health, USA) analysis software was used to calculate the average fiber diameter over 50 distinct nanofibers taken from different images of 2 NGCs conceived with similar conditions. Moreover, the fiber alignment was analyzed using the "Directionality" plugin based on the FFT function that converts the SEM image to a "frequency" space representation. Images with grayscale pixels having distributions reflecting the fiber alignment on the initial SEM images were formed. The pixel intensities were acquired as a function of direction and plotted between 0° and 180°. The degree of fiber alignment was weighed up in function of the shape and the height of the obtained curve.

In order to visualize the cross section of the NGCs, an immersion in liquid nitrogen was done prior to the sectioning and SEM imaging to avoid fiber damaging and conduit compression during the cutting procedure. In this way, precise measurements of the NGC diameter and wall thickness could be done using ImageJ.

2.4.4. AFM analysis

Atomic force microscopy (AFM) was employed in an effort to determine the macroscopic surface roughness of the inner NGC wall and the surface roughness of individual PA nanofibers before and after plasma treatment. To do so, the XE-70 AFM device (Park Scientific Instruments) was used to scan the sample surface in a non-contact mode by means of a highly doped crystal silicon cantilever having a spring constant of 40 Nm^{-1} (Nanosensors™ PPP-NCHR). In order to ultimately assess the roughness of a single nanofiber, three progressively scaled down scanning steps were performed. Firstly, untreated and plasma-treated NGCs were cut opened and the inner nanofibrous mesh was scanned over an area of 25 × 25 μm^2. In the second step, the scan domain was narrowed down to 5 × 5 μm^2. Finally, the scan area was further reduced to 500 × 500 nm^2 which is restricted to a single nanofiber. The surface roughness of the three scanned areas was then quantified using the XEI software. For each condition, three different AFM images were acquired. The obtained root mean square roughness (Rq) values are presented as the average ± standard deviation of the 3 measurement points.

2.5. Porosity measurements

The porosity of the nanofibrous mesh forming the NGC wall was determined based on the liquid displacement method [41,42]. Ethanol was selected as displacement liquid as it was shown to permeate through the porous NGC without shrinking or swelling the polymeric matrix forming the wall. The porosity percentage was calculated following Eq. (1):

$$P\,(\%) = (m_3 - m_4 - m_1)/(m_2 - m_4) \times 100 \tag{1}$$

where m_1 is the dry NGC mass, m_2 is the mass of a bottle filled with ethanol, m_3 is the mass of the bottle filled with ethanol in which the NGC was immersed and m_4 is the mass of the bottle filled with ethanol after taking out the ethanol-saturated NGC.

The porosity values are expressed as average ± standard deviation ($n = 4$).

2.6. Swelling index measurements

In order the determine the swelling index of the NGCs before and after plasma treatment, the scaffolds were firstly weighted then immersed, up to 3 days, in phosphate buffer saline (PBS; pH 7.4) at 37 °C in order to mimic the physiological body conditions. Thereafter, the NGCs were removed from the solution at different time intervals (1, 2 and 3 days) then weighted after being blot dried in a timed and consistent manner using precision wipes (Kimtech Science™) to wipe away the extra PBS. The swelling index (SI) was then calculated following Eq. (2):

$$SI = \frac{W_W - W_D}{W_D} \tag{2}$$

with W_W and W_D being the weights of the wet and dry NGCs respectively. The SI was measured on 4 different NGCs for every condition and the reported values are the average ± standard deviation.

2.7. Tensile measurements

Uniaxial testing was carried out with a Tinius Olsen tensile tester to assess the mechanical properties of the NGCs pre- and post-plasma treatment. To do so, the NGCs were cut open longitudinally and both ends (5 mm) were wrapped using a polyvinyl chloride tape with a silicone rubber adhesive material to facilitate the clamping of the ends in between two pneumatically actuated rubber grips and to hamper any potential sliding. This vertical mounting of the NGCs left a gauge length of 10 mm for the mechanical loading that was performed at room temperature with a fixed preload of 1 N and a displacement speed of 10 mm/min. Prior to the mounting, the exact wall cross-sectional thickness of each NGC was measured using a digital micrometer (Mitutoyo, Kruibeke, Belgium) on 4 random spots and averaged out. The resulting stress-strain curves were used to determine the ultimate strength at maximum load just before failure and the Young's modulus being the tensile elasticity calculated as the slope of the stress-strain curve's linear part. The reported results are the average of the values measured for 3 NGCs of each test group.

2.8. Primary SC culture studies

Primary SCs were harvested from sciatic nerves of neonatal Wistar rat pups, in compliance with the Dutch Animal Experimental Act and with the approval of the local and national ethical authority. Tissue was further processed via dissection and digestion of the nerves following the cell isolation and purification method described by Kaewkhaw et al. [43]. This method is based on the use of a selective culture medium simultaneously inhibiting fibroblast growth and favoring SCs survival and proliferation. Briefly, the harvested nerves were chopped and digested using a 0.05 % (*w/v*) collagenase solution in 5 % CO_2 for 60 min at 37 °C. The obtained cell suspension was then filtered via a 40 μm cell strainer and centrifuged for 6 min at 400 *g*. Afterwards, the supernatant was removed and the cell pellet was washed with Dulbecco's modified Eagle medium (DMEM) containing 100 U/ml penicillin/streptomycin and 10 % fetal bovine serum (FBS). Cells were centrifuged once more for 6 min at 400 g and the supernatant was discarded. Finally, SCs were resuspended and cultured in DMEM Glutamax (Cell Culture Technologies) supplemented with 10 % (*v*/*v*) FBS, 0.25 μg/ml amphotericin B, 1 % (v/v) N2 supplement (R&D Systems), 20 μg/ml bovine pituitary extract, 1 % (v/v) penicillin/streptomycin and 5 μM forskolin (Sigma-Aldrich). Cell cultures were kept at 37 °C in a humidified environment containing 5 % CO_2. The medium was refreshed every 3 days and SCs were subcultured once they got to 80 % confluency.

2.8.1. Cell seeding on the NGCs

Before cell seeding, UV-sterilized PA conduits were longitudinally cut open in two to generate flat electrospun sheets. Each sheet was placed in a rectangular well (8 mm × 2 mm) made up of polydimethylsiloxane (PDMS) from the Sylgard 84 elastomer kit (Dow Corning). In order to create the PDMS wells, a mixture of the elastomer and the curing agent was prepared at a ratio of 10/1 (*w*/w) and filled inside rectangular molds having the desired dimensions. Afterwards, the mixture was degassed in a vacuum chamber. The curing process was done in an oven at a temperature of 80 °C for 1 h. The resulting PDMS casts were removed from the molds and dry-sterilized in an oven at a temperature of 160 °C for 4 h. In order to prevent cell attachment on the PDMS casts and constrict it on the NGCs, a solution of 0.5 % Pluronic F127 was poured in each PDMS well. After 30 min of incubation, the wells were washed 2 times with phosphate-buffered saline (PBS).

Once the untreated and plasma-treated PA NGCs were placed in the PDMS wells, an incubation in DMEM supplemented with 10 % FBS was done overnight. The medium was then removed and the NGCs were washed 2 times with PBS. SCs of passage 6 and 7 were seeded, at a density of 30,000 cells/cm^2, on the NGCs. Two sets of experiments were performed in which SC culturing was done using either a medium without FBS or a medium containing 10 % FBS. In this way, one can evaluate if cells would sense plasma-induced surface changes similarly in the absence or presence of the FBS proteins in the medium. The common constituents of both media were the following: DMEM Glutamax, 1 % horse serum, 2 % N21-MAX supplement (R&D Systems), 100 ng/ml of recombinant human NGF-β (Sigma-Aldrich) and 1 % penicillin/streptomycin. Cellular behavior was evaluated at day 1, 3 and 7 after seeding. Both sets of experiments were repeated 2 times each and in all 4 sets, 2 samples per condition were considered for every assay.

2.8.2. Immunostaining and fluorescence microscopy

Cells cultured on PA NGCs were fixed with 4 % (*v*/v) paraformaldehyde (Sigma-Aldrich) in PBS for 20 min at a temperature of 4 °C. Afterwards, the permeabilization of the fixed cells was done using 0.1 % (v/v) TritonX (Sigma-Aldrich) in PBS for 15 min at ambient temperature. A blocking step followed via the immersion of the samples in a blocking buffer composed of 0.05 % Tween-20 (VWR), 5 % goat serum (Sigma-Aldrich) and 1 % bovine serum albumin (BSA, VWR) in PBS for 1 h at room temperature. NGCs were then incubated overnight in a primary antibody solution of rabbit anti-S100 antibodies (1:1000; Sigma-Aldrich) at a temperature of 4 °C. The samples were subsequently washed using a solution composed of 1 % BSA and 0.05 % Tween-20 and incubated for 1 h at ambient temperature with anti-rabbit Alexa 488 antibodies produced in goat (Invitrogen). The NGCs were finally washed with PBS and mounted using Mowial 4-88 (Sigma-Aldrich) on microscope slides that were stored at 4 °C until imaging. SCs were visualized by fluorescence microscopy making use of a Nikon Eclipse Ti2 inverted microscope and images of the 4 different NGC zones were acquired at a magnification of 20×. Moreover, an automated stitching of overlapping images (12 × 1; 10× magnification) was also performed in order to visualize the cells on the full NGC length.

2.8.3. Fluorescent image analyses

Before analysis, all fluorescent images were subjected to automated background subtraction and local contrast enhancement given the fact that the electropsun scaffolds were showing a low degree of autofluorescence leading to the appearance of a light background color. To do so, the command “Subtract background” of ImageJ was used with a rolling ball radius of 100 pixels. Thereafter, the command “Enhance Local Contrast (CLAHE)” was employed with a blocksize, histogram bins and maximum slope of 127, 256 and 3.00 respectively. The distribution of SCs along untreated and plasma-treated NGCs was quantified by first converting the stitched images to binary images and then plotting the fluorescent intensity profile as a function of the position on the NGC. Moreover, the average fluorescent intensity of each NGC zone was calculated. The individual images were also converted to binary images and used to measure the circularity of the cells on the different zones of the NGCs using the automatic command “Analyze particles”. A circularity value of 1 is actually indicative of perfectly circular cells. The more the value approaches 0, the more the cells are elongated. The presented data were taken from 4 different images of each zone.

2.8.4. SC fixation protocol for SEM analysis

Next to the immunofluorescent images, SC-seeded NGCs were visualized by means of SEM imaging. To do so, SCs were firstly fixed by incubating the NGCs in 4 % paraformaldehyde for 20 min at 4 °C. A dehydration step was then carried out by immersing the samples in a series of escalating ethanol concentrations (50 %, 70 %, 85 %, 95 % and 2 × 100 %) for 10 min/immersion. Thereafter, NGCs were soaked in hexamethyldisilazane (HMDS), left to dry under the fume hood, gold sputter-coated and imaged at an accelerating voltage of 7 kV.

2.9. Statistical analyses

The obtained ultimate stress, Young's modulus, average fluorescent intensity and cell circularity data were subjected to a statistical analysis implicating one-way Anova and Turkey post-hoc tests. A significance level of $P < 0.05$ was adopted.

3. Results and discussion

3.1. *Characterization of the electrospun PA NGCs*

After electrospinning, the deposited PEOT/PBT fibrous network was successfully pulled out from the tubular mandrel to obtain a steady NGC not showing any signs of collapse all over its length (Fig. 2 A). After SEM examination, the electrospun NGCs showed an inner diameter of 2 mm and a wall thickness of 200 μm (Fig. 2 B). The wall thickness was purposely conceived to be almost 2 times bigger than the one considered in several previous studies because the nerve defect that is intended to be repaired is bigger (2 cm) and requires a steady bridging for a longer time [4,18].

When taking a closer look at the inner and outer walls, one could notice consistently well-shaped and smooth fibers with diameters of 710 ± 98 nm and 775 ± 83 nm respectively (Fig. 2 B). In fact, this range of fiber diameter, previously shown to engender desired nerve and glial cell performances, was specifically aimed at by testing different polymer concentrations of the electrospinning solution [44,45]. Wang et al. reported that fibers having a closely matching diameter (759 nm) exhibited the extension of the longest neurites from dorsal root ganglia explants compared to fibers with smaller (293 nm) and larger diameters (1325 nm) [44]. Moreover, after evaluating the influence of different fiber diameters in the range of 340–1306 nm on SC behavior, Gnavi et al. concluded that: 1) thinner nanofibers promote SC spreading and cytoskeleton organization which enhance cell adhesion and proliferation rate; 2) thicker microfibers boost SC motility and stretching which heighten cellular migration rate [45]. Therefore, a trade-off implicating an intermediate fiber diameter is believed to synergistically activate SC adhesion, proliferation and migration. Fig. 2 C, depicting the fiber diameter distributions on the inner and outer walls of the NGCs, roughly reveals normal distributions with no fiber diameters below 500 nm or above 1050 nm thus showing an acceptable fiber diameter homogeneity. Next to the importance of the diameter, the fiber orientation also critically influences glial and neural cell behavior. A clear difference between the inner and the outer walls was observed: bundles of aligned fibers with random fibers in between composed the inner wall, while randomly deposited fibers completely formed the outer wall (Fig. 2 B). This observation was quantitatively confirmed by generating the Fast Fourier Transform (FFT) output images and plotting the pixel intensity in function of the fiber direction (Fig. 2 C). Results showed that the inner wall displayed a significantly narrower and higher distribution curve compared to the outer wall thus corroborating the considerable heightening of the inner fiber alignment and the outer fiber randomness. The fiber alignment was previously shown to play a crucial role in achieving an efficient nerve regeneration with a certain degree of functional recovery by triggering SC guided migration and bipolar morphology [5,9,17,46]. However, the absence of pores in between highly aligned fibers is accompanied with a limitation illustrated by the hindrance of the crucial nutrient penetration inside the NGCs. The

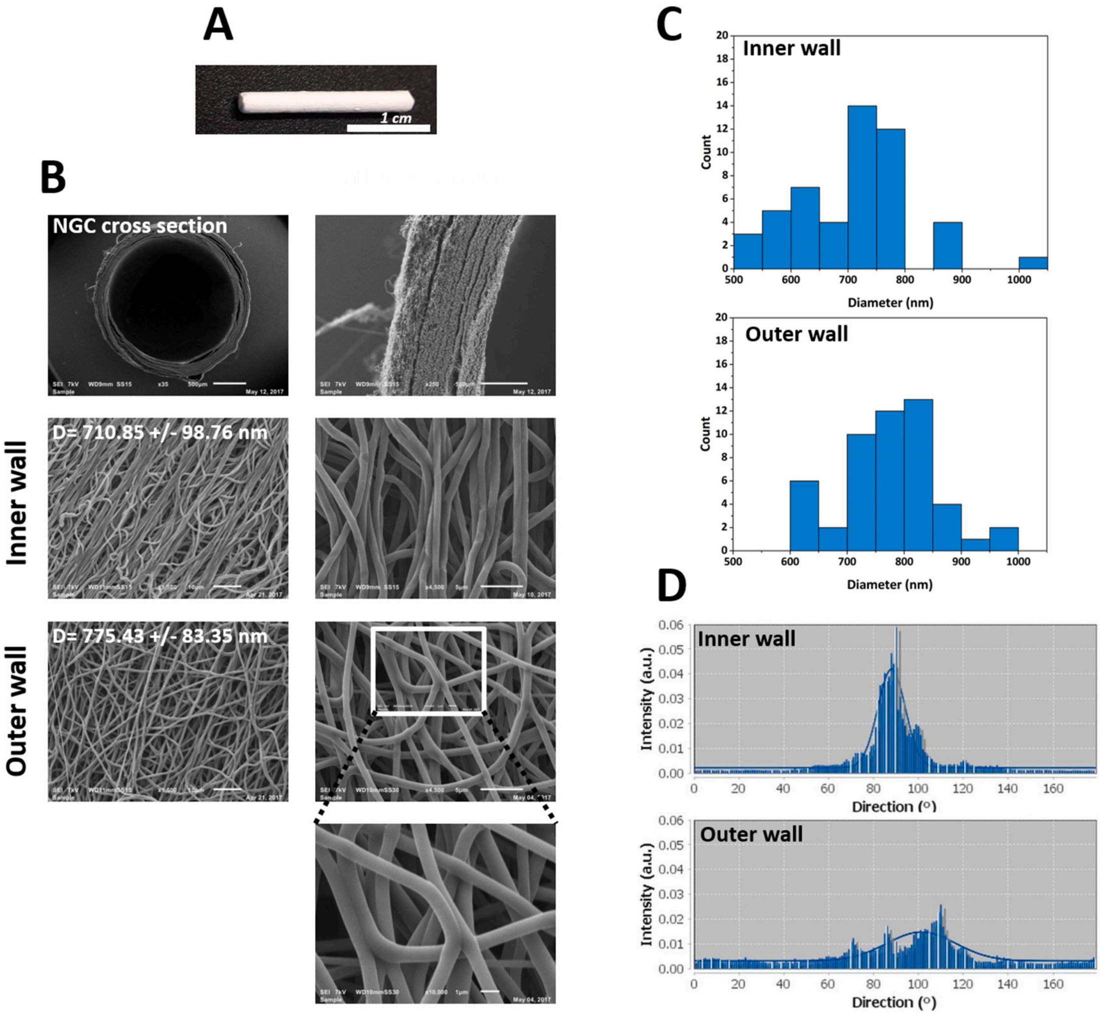

Fig. 2. A: Photograph of the obtained NGC (length: 2 cm); B: SEM images of the NGC cross section (magnification: 35×), the wall cross section (magnification: 250×) and the fibers on the inner and outer NGC walls (magnifications: 1500×, 4500× and 10,000×); C: Bar plot of the fiber diameter distribution on the inner and outer NGC walls; D: FFT pixel intensity plot in function of fiber direction on the inner and outer NGC walls.

presence of random fibers with interconnected pores intercalated in between the aligned fibers on the inner wall came to solve this issue. This beneficial inner wall architecture, synergistically enhancing a SC elongation and migration while allowing nutrient exchange, was never observed, to the best of our knowledge, in any of the previously engineered NGCs nor in the wide electrospinning literature in general. The outer wall architecture presenting a higher porosity is expected to further intensify the influx of trophic factors that are expected to concentrate inside the NGC thus creating a more regenerative microenvironment. This boosted nutrient inflow is extra-needed in long nerve gaps since the regenerative capabilities of the nerve ends can be exceeded [4]. In fact, when measuring the porosity of the NGC wall by means of the liquid displacement method, a high value of 89.28 +/− 2.38 % was obtained thus classifying the NGCs into the highly porous scaffold category. Comparable results were detected in literature when measuring the porosity of electrospun nanofibers using the same method. For instance, Sadeghi et al. reported a porosity of 93 % for chondroitin sulfate nanofibers having a mean diameter of 388 nm [42]. This slightly higher porosity is due to the lower fiber diameter compared to the NGC nanofiber diameter given the fact that when the fiber diameter rises, the porosity normally decreases [41]. Despite a lower mean fiber diameter of 415 nm, Liu et al. obtained a slightly lower porosity of 85 % for aligned PCL nanofibers compared to the porosity of the NGC wall [47]. This again reveals the added value of the inner wall architecture characterized by a mix of bundle of aligned fibers with random fibers in between in enhancing the NGC's porosity. Moreover, the presence of random fibers on the outer wall safeguarded for the steady bridging role of the NGCs thanks to their numerous joining points forming a robust fibrous network. This network strengthens the complete conduit structure and prevents the fibers from falling apart. A higher SEM image magnification (10,000×) revealed that overlapping fibers of the outer wall were slightly fused together, thus consolidating more the NGCs (Fig. 2 B). This fiber fusion was attributed to the retention of small solvent amounts that merged fibers in contact when depositing on the tubular collector and formed a number of physical cross-links after complete solvent evaporation. Another advantage of the random deposition of fibers on the outer wall is the enhanced tear resistance that it appends to the entire wall. This makes the NGC more prone to withstand the surgical coaptation where a suture travels through the NGC wall multiple times to secure it to the nerve stumps [2].

The distinctive NGC double-layered wall obtained in this study was generated in a one-step electrospinning process with custom-tailored parameters. Since the goal was to align the inner fibers along the conduit length and not perpendicular to the tubular mandrel, a very low mandrel rotational speed of 50 rpm was put into play during electrospinning. In this way, the mechanical forces caused by high speeds stretching and aligning the fibers in the same motion direction were partly cancelled out. Next to decreasing the rotational speed, all the device parts neighboring the mandrel were covered with an insulating tape, thus giving prominence to the metallic mandrel conductivity. Therefore, the charged fibers were driven by electrostatic forces to stretch and deposit in an aligned manner spanning the mandrel length. Yet, the rotation of the collector was probably still interrupting this electrical effect by imposing a mechanical force that disrupted the continuity of the fiber alignment on the complete wall circumference and led to the deposition of interspersed random fibers. The more the metallic mandrel was covered by the non-conductive polymeric fibers, the less the electrical forces causing the alignment were intervening thus leading to randomly deposited fibers on the outer layers. In previous studies involving electrospun NGCs, few researchers generated double-layered scaffolds of aligned and random fibers by rolling and securing 2 fibrous sheets into a cylindrical shape [2,15,17]. However, the fabrication of seamless bi-layered NGCs presenting an even and smooth luminal wall and eradicating the risks of mechanical failure and seam dissociation was rarely performed. In most studies implicating the electrospinning of NGCs on a tubular mandrel in a simple one-step procedure, walls composed of only random fibers were mainly formed [18,48]. To our knowledge, Zhu et al. were the only ones to successfully electrospin bi-layered NGCs by adopting this simple approach. However, highly aligned fibers lacking the mandatory porosity for nutrient supply were formed on the inner wall [14].

3.2. XPS analysis pre- and post-plasma treatments

3.2.1. Survey scans: elemental composition

After electrospinning, XPS measurements were carried out to assess the surface chemical composition of the NGCs. Since SCs will be in direct contact with the inner wall, the measurements that follow were only restricted to the inner NGC surface. XPS survey scan analysis revealed a surface oxygen content of 17.5 % and a C-content of 82.5 % on the 4 different zones of the NGC thus indicating a homogeneous surface chemistry across its length (Fig. 3 A).

In an attempt to enhance the surface chemical properties for improved SC activities, the NGCs were subjected to different plasma treatments. In a first set of experiments, a DBD operating in air or in Ar at medium pressure was used for this purpose. In contrast to 2D surfaces, plasma modification of 3D scaffolds using a parallel plate DBD is a challenging task since plasma penetration through the interconnected pores is required to efficiently treat the inner wall. Therefore, in order to precisely evaluate the plasma capacity to reach and modify the luminal surface, XPS measurements were performed on NGCs exposed to different plasma treatment times (Fig. 3 A). Results showed that air and Ar discharges lead to different chemical surface modifications along the NGCs. After 2 s of plasma exposure, almost no changes in the NGC surface chemistry were detected when Ar was used as discharge gas. However, a significant increase in oxygen content from 17.5 % to at least 20.9 % could already be detected when air was used as discharge gas, thus highlighting the fast penetration of air plasma inside the NGCs. Nevertheless, the conduits were non-homogeneously treated since the oxygen percentage was shown to vary along the NGCs. In return, the surface C-content decreased proportionally with respect to the oxygen increase since no other elements were incorporated on the fiber surface during or post-plasma treatment. When increasing the plasma exposure time to 4 s and 8 s, a sudden increase in the surface oxygen from 17.5 % to around 23.6 % and 24.7 % respectively was perceived in case of the Ar discharge. These results also denoted the penetration ability of Ar plasma but with a delay compared to air plasma. Moreover, it is worth mentioning that Ar plasma engendered a completely homogeneous surface modification illustrated by similar oxygen percentages on the 4 zones along the luminal wall. In the air discharge, the oxygen content continued to increase after 4 s and 8 s of treatment time but in smaller steps and with the same non-uniform trend across the NGC length. A plasma exposure time of 16 s marked a noticeably higher and uniform oxygen incorporation reaching around 28 % along the NGCs treated with Ar. This percentage could not be attained with the air discharge where zones 1, 2 and 3 continued to incorporate less oxygen (≈ 25 %) than zone 4 (≈ 27 %). At 32 s of plasma exposure, a saturation of the treatment effect was distinguished in both discharges as the NGC surface chemistry was analogous to the one detected at a 16 s treatment.

In order to get a clear understanding on how air and Ar plasmas modified differently the NGC inner wall, it is essential to elucidate: 1) the mechanisms underlying plasma penetration throughout the NGC wall thickness and 2) the effects of each discharge atmosphere on the different active species bombarding the fibrous surface. First, the active species of plasma generated between both DBD electrodes must have the chance to move to the intended reaction location, which is the inner NGC wall without losing their modifying capacity. This diffusive transport of particles is mainly influenced by their mean free path on the one hand and the fibers inter-distance or the wall porosity on the other hand. When the mean free path of the surface modifying particles is smaller than the typical distance between PA fibers, the particles are more prone to collide with each other rather than with the NGC. However, when the

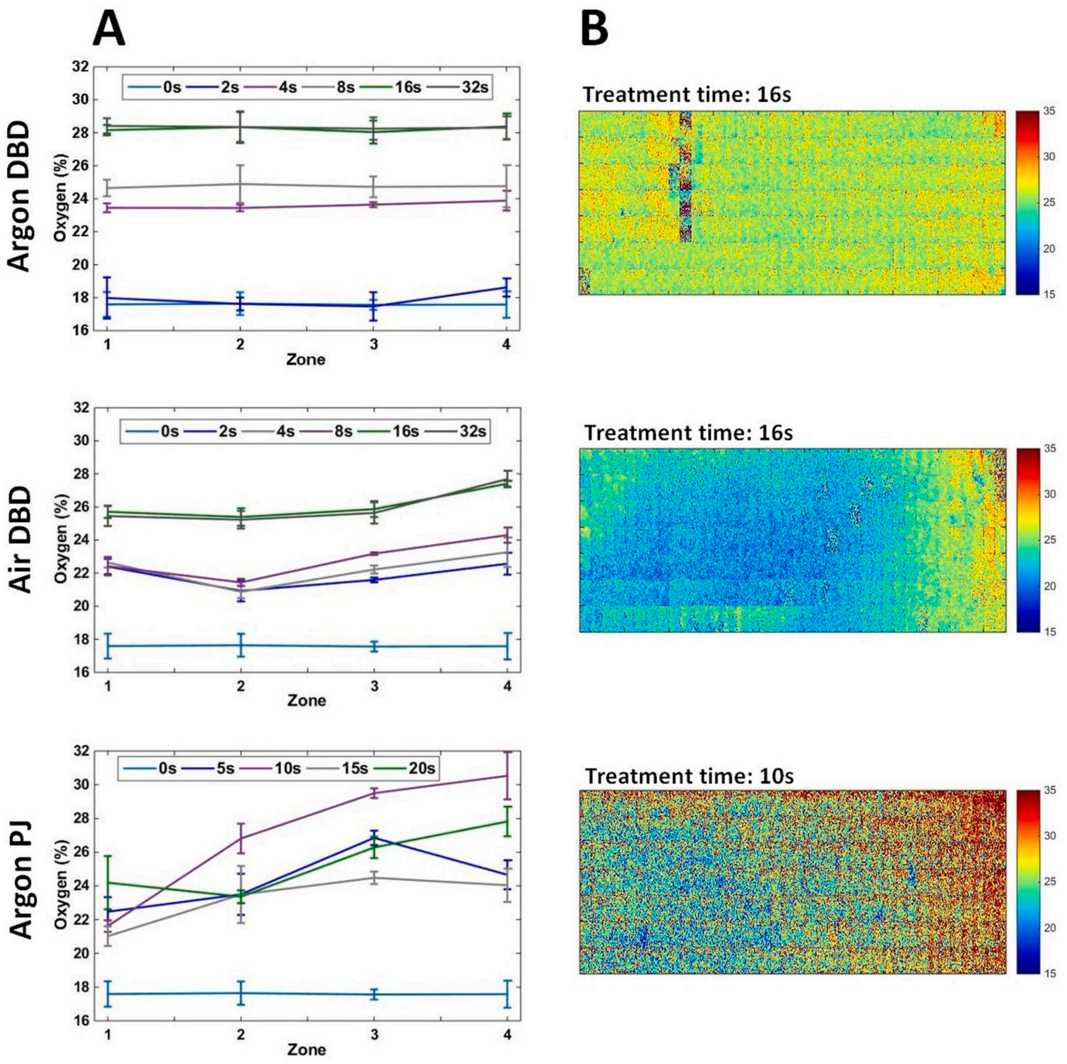

Fig. 3. A: Evolution of the surface oxygen content on 4 zones of NGCs subjected to argon DBD, air DBD and argon PJ treatments as function of plasma exposure time. B: XPS micro-mapping images of the oxygen distribution on the complete inner surface of NGCs subjected to air DBD, Ar DBD and Ar PJ treatment at specific treatment times.

mean free path is comparable to or bigger than the wall pore size, plasma species impact only with the NGC surface and the shortfalls of particles induced by excessive collisions are ignored [49,50]. Since Ar is denser than air, one can deduce that the active species in air plasma had bigger mean free paths than the ones in Ar plasma. This can explain the faster penetration of air plasma (2 s) inside the NGCs. The pressure in which plasma is generated also plays a decisive role in the particles' diffusive transport as it substantially influences the mean free path of plasma species. It was actually stated that the optimal pressure range for plasma modification of the full thickness of multilayered textiles is restricted between 0.1 and 10 kPa [50]. Since the DBD plasma treatments performed in this study were conducted at a medium pressure of 5 kPa, the active species seemed to attain sufficiently large mean free paths to be able to reach the luminal wall. This is why Ar plasma could also modify the inner wall surface but with a slightly delayed primary effect (4 s). It is worth mentioning that the inner wall architecture presenting interfibrous pores due to the partial presence of random fibers instead of only aligned fibers also played a role in the successful penetration of plasma species into the lumen.

Once inside the NGC, 2 types of species are recognized to induce surface chemical changes: 1) non-reactive species break down C—H and C—C bonds spawning surface radicals and 2) chemically reactive species such as molecular and atomic oxygen insert new functional groups. Since one of the plasma treatment is sustained in pure Ar, the grafting of oxygen-containing functionalities should not theoretically occur and the generated radicals should instead interact with each other forming a cross-linked network [21,51]. In reality, the plasma chamber contains oxygen impurities sourced from: 1) gaseous components such as H_2O and O_2 that plasma desorbs from the reactor walls, 2) oxygen traces in the working gas, 3) air remaining in the plasma chamber because of insufficient pre-treatment pumping and evacuation. Moreover, post-treatment oxidation via secondary reaction pathways between the plasma-created radicals and oxygen molecules of the surrounding air is also anticipated to take place [26,52].

For the sake of testing if plasma species lost some of their surface modification ability during the penetration throughout the NGC wall, flat PA fibrous membranes were plasma-treated and a comparative XPS analysis was performed. Maximal oxygen contents of 28.4 % and 28.7 % were detected on the surfaces treated with air and Ar DBD respectively. These results revealed the fact that air plasma was unable to modify the inner NGC wall with its full potential like Ar plasma. The reason behind these distinctive consequences is presumably the different DBD modes being filamentary and glow in the air and Ar discharges respectively. A higher concentration and more even distribution of surface modifying species and ions are normally present in the glow mode compared to the filamentary mode [53]. Therefore, even if some particle losses occurred during the movement throughout the NGC walls, a higher amount of species responsible for the surface modification would reach and concentrate in the lumen in case of the glow Ar discharge. This can explain why the middle NGC zone could only incorporate around 25 % of oxygen in the air discharge while 28 % of oxygen was incorporated in the Ar discharge.

The inhomogeneous surface modification of the air plasma-treated NGCs showing a higher oxygen content (27.4 %) on zone 4 is probably due to the side penetration of plasma through the conduit opening. This occurred only at the NGC side positioned next to the gas flow inlet. This "gradient-like" oxygen content created along the NGCs can be interesting in enhancing nerve regeneration as regrowing axons were shown to be driven by chemotactic signals distributed in a spatial concentration gradient [33]. However, a "real" and steeper gradient with increasing oxygen content on each of the 4 zones is more likely to obtain this beneficial effect. Therefore, in a trial aiming at generating such a gradient, the NGCs were subjected to a PJ treatment operating in Ar at atmospheric pressure. In this way, the plasma jet or the so-called effluent plasma outflew from the jet capillary and directly penetrated inside the NGC through its opening. Ideally, a gradual decrease in the plasma intensity was supposed to occur across the effluent length leading, in theory, to a gradual decrease in the plasma modification efficiency along the NGC surface. Nevertheless, after 5 s of plasma exposure, the oxygen content increased in an arbitrary manner from 17.5 % to 22.4 %, 23.5 %, 26.8 % and 24.6 % on zone 1 to 4 respectively (Fig. 3 A). An unbalanced and non-gradient oxygen incorporation was also previously perceived when treating polyethylene tubes making use of an atmospheric pressure argon PJ [40]. This fluctuating behavior is probably due to very specific gas-dynamic processes occurring at the inlet region. Moreover, another explanation might be related to the theory stating that the PJ discharges are particularly comprised of a train of ionization waves propagating at high speeds and known as "plasma bullets" [54]. Many studies have noted the complicated mechanisms underlying the propagation of "plasma bullets". One of the assumptions indicated that the electron density distribution, the electric field and the active species inside a bullet are non-homogeneous [55–59]. When increasing the treatment time to 10 s, a gradient incorporation of oxygen was successfully attained along the NGC with a 9 % difference between the lowest and the highest amount (zone 1: 21.6 %; zone 2: 26.8 %, zone 3: 29.5 %; zone 4: 30.5 %). This is presumably attributable to the plasma propagation that started after a certain treatment time to follow a more controlled trend: the radius of the bullets increased progressively along the NGC path while plasma intensity decreased affecting less and less the surface [40]. When increasing the treatment time even more to 15 s and 20 s, fluctuations in the oxygen amount were again perceived along the NGCs with an overall average drop. Most likely, this behavior could be correlated with the plasma etching effect that started to cause at extended treatment times a random depletion of the plasma-induced oxygen containing bonds and the bonds already present in the polymer backbone. Although mainly triggered by the presence of oxygen species, the etching effect was also observed in Ar plasmas where UV etching is predominant over the oxidative degradation [26,60,61]. Riekering et al. also perceived a decrease in the O/C ratio when subjecting PEO/PBT films to an Ar plasma treatment at a certain exposure time [60]. This outcome was linked back to the preferential etching of the softer PEO regions of the copolymer that was also anticipated to take place during PJ treatment of the NGCs in this present study.

In what follows, the analysis will be restricted to the optimal plasma exposure times: argon DBD treatment of 16 s, air DBD treatment of 16 s and argon PJ treatment of 10 s.

3.2.2. XPS micro-mapping

After assessing the surface elemental composition on the 4 different zones of the plasma-treated NGCs, an advanced and uncommon XPS micro-mapping was performed to visualize with great precision the exact distribution of oxygen over the complete NGC inner wall surface. In this way, the homogeneous and gradient surface modifications induced by the different plasma treatments could be confirmed and further highlighted. The obtained XPS micro-maps (1900 × 350 values) are displayed in Fig. 3 B. Since oxygen and carbon are the only elements present on the NGC surface, the maps showing the C-content are not presented as they picture the reverse of the oxygen maps. Ar DBD provided a completely homogeneous surface modification, thus corroborating the previous zone-specific results. An overall lower and non-homogeneous oxygen incorporation was observed after air DBD treatment underlying again the reduced amount and efficiency of plasma species penetrating throughout the NGC wall and interacting with the inner surface. The map exposed a "gradient-like" distribution illustrated by a noticeable increase in the oxygen content on a quarter area at one side of the NGC. This particular observation ascertained our previous assumption concerning the side penetration of plasma through the NGC opening close to the gas inlet, leading to a more efficient surface modification on one extremity. Finally, a steep gradient map with increasing oxygen content along the NGC length was clearly discerned post-argon PJ treatment to be in line with the previous zonal analysis. In this way, a new approach involving a simple PJ design was used to create a chemical gradient in tubular scaffolds. Previous studies aiming at creating chemical plasma gradients on polymeric surfaces were only applied on 2D films using very complex and extensively redesigned plasma reactors involving for instance automated stepper motors moving the samples, reshaped electrodes and shielding covers [62,63]. No study has reported so far the formation of a surface plasma chemistry gradient inside NGCs. The few authors that have implemented luminal growth factor gradients on NGCs did not carry out any advanced (XPS micro-mapping) or even basic chemical characterizations thus not being able to fully understand the resulting cellular behaviors that are to a large extent influenced by the underlying surface chemistry [5,33]. Overall, a visual comparison between the 3 maps draws more attention to the big variances that can be induced by different working gases and reactor configurations in the plasma treatment of electrospun tubular scaffolds.

3.2.3. C1s peak deconvolution: chemical bonds

In order to get an insight on the specific types and relative amounts of the plasma introduced oxygen-containing functionalities, high resolution C1s curves were deconvoluted for each of the 4 NGC zones. According to the molecular structure of PEOT/PBT and to literature, the C1s envelope of the copolymer encompasses 4 different peaks: a peak at 285.0 eV attributed to hydrocarbon and aliphatic or aromatic carbon bonds (C—C), a peak at 286.5 eV ascribed to hydroxyl groups (C—O), a peak at 287.7 eV accredited to carbonyl groups (C=O) and a peak at 289.1 eV corresponding to carboxyl groups (O-C=O) [25,64]. A table that contains the quantitative results of the C1s fitting carried out for untreated NGCs and for the 4 zones of NGCs subjected to air DBD, Ar DBD and Ar PJ treatments can be found in the supporting information (Table S1). In order to have a more evident comparison between the untreated and the different plasma-treated NGCs, the mean fold change of the relative concentrations of the different functionalities was calculated for the 4 zones of the plasma-treated NGCs with respect to their corresponding values on the untreated NGCs (Fig. 4). High-resolution C1s curve deconvolution on only zone 4 of the untreated and plasma-treated NGCs can be found in the supporting information (S2.1). The relative amount of the peak at 285.0 eV on the untreated NGCs (69.3 %) was higher by approximately 5 and 9 % than the one previously detected on spin-coated and 3D printed 300PEOT55PBT45 respectively [25,52]. In return, the total amount of the other oxygen-containing bonds was lower but their relative concentrations followed parallel proportions. This might be due to the possible enrichment of low binding energy functionalities such as methyl groups on the fiber surface over the bulk during electrospinning. After Ar DBD treatment, the relative concentration of all bonds changed substantially but similarly on all zones which is in agreement with the homogeneous oxygen

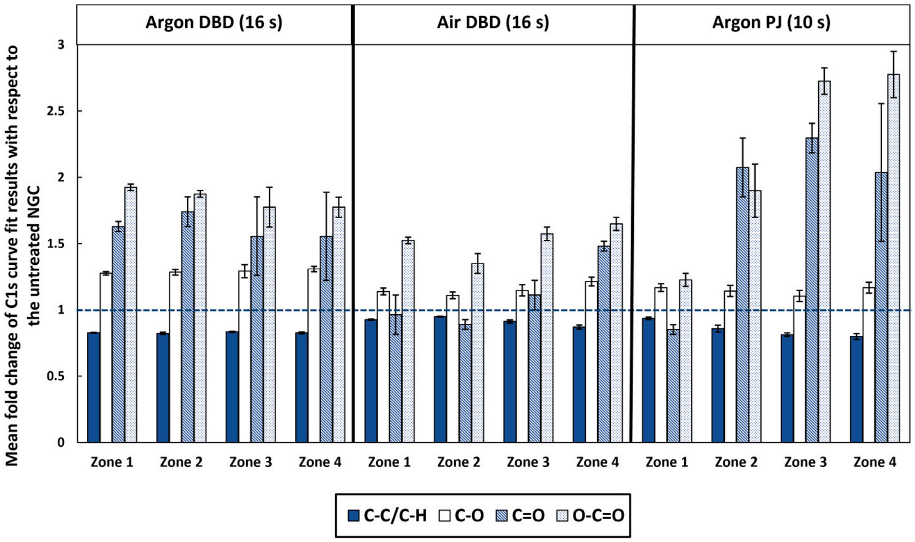

Fig. 4. Bar plot of the mean fold change of the relative concentrations of carbon-containing functionalities on the 4 zones of the plasma-treated NGCs with respect to the untreated NGC (dotted line).

incorporation on the complete NGCs. An average fold decrease (with respect to the untreated NGC) of 0.83 was noted for the C—C peak and fold changes of 1.29, 1.62 and 1.84 were detected for the C—O, C═O and O-C=O peaks respectively. These results suggest that Ar plasma attacked C—C and C—H bonds and the formed radicals could interact with oxygen species rather than fully undergoing cross-linking. The C—O bonds (31 %) were shown to be more easily incorporated than O-C=O (7 %) and C═O (4 %) bonds, which was frequently observed after Ar plasma treatment of some other polymers [61,65]. Air DBD treatment also induced noticeable variations in the C1s curve fit but to a lower extent and in a non-homogeneous manner over the NGC length. As anticipated, zone 4 showed the largest changes as it was affected by the side plasma penetration. A mean fold decrease ranging between 0.87 and 0.95 was noted for the C—C peak and fold changes ranging between 1.11 & 1.21, 0.90 & 1.48 and 1.35 & 1.65 were detected along the NGCs for the C—O, C═O and O-C=O peaks respectively. Given the reduced potential of air plasma species in modifying the surface after crossing the NGC wall, C═O groups were not introduced at all on zones 1 to 3. This result was to be expected as a normal air DBD plasma treatment of flat PEOT/PBT films was previously shown to have a lower ability in incorporating C═O groups than an Ar DBD treatment [52]. Interestingly, a remarkable gradual decrease in the mean fold change of C—C bonds from 0.93 to 0.79 and a prominent continual increase in the mean fold change of O-C=O bonds from 1.22 to 2.77 were detected along the NGCs subjected to Ar PJ treatment. These ascending and descending changes were in line with the surface oxygen and carbon gradients revealed by the XPS survey scans and micro-mappings. No signs of C═O bond incorporation were detected on zone 1, while zones 2 to 4 showed an average C═O fold change of 2.14 with respect to the untreated NGC. Despite the overall higher surface modification potential of the PJ compared to the DBD, the maximal C—O bond amount found after Ar DBD treatment was not attained after PJ treatment. Moreover, the C—O fold change to the untreated NGC was not homogeneous on the different zones of the PJ-treated NGCs nor following a gradient trend of increasing values along the NGC. Since the PJ operated at higher power, this behavior is presumably linked to the preferential plasma etching of the softer PEOT segments causing the depletion of C—O bonds from the polymer backbone. This depletion was overcompensated by the incorporation of new C—O bonds that could not reach at the end the amount added during DBD treatment. This elucidation can be further approved by several studies showing a stagnation or even a decrease in C—O bonds on the surface of PEOT/PBT samples after plasma activation making use of reactors with higher powers [25,52].

3.3. Surface wettability and swelling index pre-and post-plasma treatments

The grafting of the aforementioned polar functionalities on the plasma-treated NGCs is well-known to boost their surface wettability which is recognized to play a primordial role in enhancing SC adhesion and proliferation [66]. Therefore, the wettability of the inner wall surface of the NGCs was assessed via WCA measurements performed on the 4 pre-defined zones. Given the fact that the obtained WCA values on all zones of every condition did not show any statistical difference, the results reported in Table 1 represent the average WCA values measured on the whole NGC length. The starting WCA on the untreated NGC was 95° which could situate it into the hydrophobic category. A considerably lower WCA value of 59° was previously detected on untreated 300PEOT55PBT45 films [52]. On the one hand, this difference might be due to the potential enrichment of low binding energy functionalities such as C—C groups on the fiber surface over the bulk during electrospinning at the expenses of polar oxygen-containing functionalities. On the other hand, amplified hydrophobicity is always perceived on 3D nanofibrous meshes compared to 2D surfaces. This is attributed to the topography of nanofibers exhibiting numerous inter-fiber pores in which the ambient air ends up entrapping thus partially hindering water infiltration [26]. When exposing the NGCs to the different plasma treatments namely Ar DBD, air DBD and Ar PJ, an instantaneous complete infiltration of the water drop into the inner wall was spotted which led to WCAs of 0° along the NGCs regardless of the amount of

Table 1
WCA and swelling index results of the NGCs pre- and post-plasma treatments.

		NGC condition			
		No treatment	Argon DBD treatment	Air DBD treatment	Argon PJ treatment
WCA (°)		95.03 ± 3.77	0	0	0
Swelling index	Day 1	2.57 ± 0.23	2.45 ± 0.21	2.55 ± 0.11	2.61 ± 0.16
	Day 2	2.65 ± 0.27	2.48 ± 0.27	2.59 ± 0.10	2.55 ± 0.09
	Day 3	2.65 ± 0.30	2.49 ± 0.29	2.47 ± 0.18	2.44 ± 0.09

incorporated surface oxygen. In fact, when a certain threshold of chemical polarity is attained, the low tension water drop fully overpowers the air entrapment by its incapability to be held on the nanofibers surface anymore and as such completely penetrates into the inner wall turning it into a super-hydrophilic mesh [21]. This chemistry threshold was apparently reached when the surface oxygen content reached a value of 21.6 % which was detected on zone 1 of the PJ-treated NGC. This can explain the homogeneous hydro-properties along the NGCs exhibiting a plasma-induced chemistry gradient.

Next to the importance of the surface wettability of the NGCs, their swelling behavior is an important parameter to be tested. In fact, the water absorption capability of the NGCs is a vital feature since water storage and transmission throughout their wall are imperative for easy fluid exchange and appropriate cell nutrition and signaling establishment [67]. Nonetheless, although important, the swelling degree of NGCs should be moderate not to compress the regenerating nerves [10]. As such, the swelling index of the untreated and plasma-treated NGCs was assessed after immersing them in PBS at 37 °C up to 3 days (Table 1). The obtained swelling indexes of the untreated NGCs were 2.57 and 2.65 at day 1 and 3 post-immersion respectively. Since the mean values were not statistically different, one can assume that a swollen equilibrium state was already attained during the first day of immersion in PBS. This early attainment of the equilibrium state is beneficial in case of NGCs as nerve regeneration takes more time and as such regenerating nerves would not undergo any swelling-related compression. Moreover, the obtained swelling values are considered to be moderate in comparison with previously reported swelling indexes of NGCs. For instance, mass swelling indexes above 8, 5 and 6 were reported for polyethylene glycol, poly(lactic-*co*-glycolic acid) (ratio 75:25) and alginate-collagen NGCs respectively [68–70]. Swelling mechanisms require the ability of the polymeric chains to soak up water molecules across the NGC wall. In case of PEOT/PBT, the swelling capacity is attributed to the hydrophilic nature of the soft PEO segments [71]. Despite the enhanced surface wettability of the plasma-treated NGCs, unchanged swelling indexes were detected after the different treatments. This is probably due to the fact that the plasma-induced incorporation of polar groups was only limited the top surface of the nanofibers (few nanometers in depth). Therefore, the ensuing changes in water absorption and as such swelling were not detectable.

3.4. SEM and porosity analyses pre- and post-plasma treatments

Besides the advantageous surface chemical modification, the preservation of the fibrous wall morphology and porosity is an extra critical consideration to approve plasma treatment suitability for PA NGCs. Therefore, SEM images of the inner NGC wall were acquired before and after plasma treatment (Fig. 5 A). The analysis was restricted to zone 4 as it underwent the most pronounced chemical modifications in case of air DBD and PJ treatments and was therefore the most prone to plasma-induced physical damages. The 3 different plasma treatments were shown to exhibit no alterations in the morphological features of the fibers composing the NGC wall. Moreover, the particular fiber architecture illustrated by bundles of aligned fibers with random fibers in between was preserved. Since the fiber diameter is also a critical parameter influencing neural and glial performances, it was again measured post-plasma treatments [44,45]. The obtained values did not reveal any statistical differences, which also pointed out the conservation of the fiber scale even in case of PJ treatment where a mild chemical etching was probably taking place. These unchanged fiber diameter and morphology led to an unaltered high wall porosity that remained

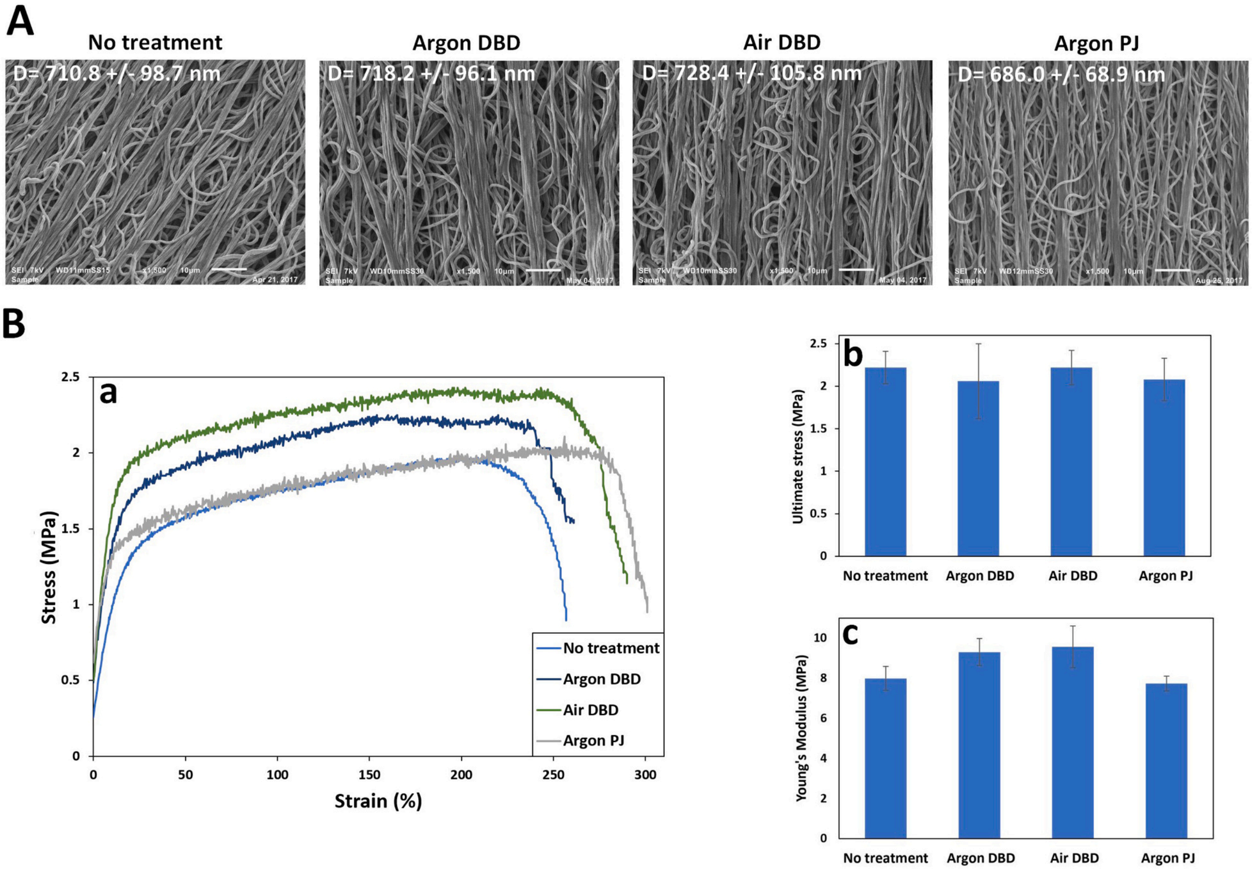

Fig. 5. A) SEM images of the inner NGC wall pre- and post-plasma treatments (zone 4 -magnification: 1500×); B) Mechanical properties of the NGCs pre- and post-plasma treatments: a. Typical stress-strain curves; b. Bar plot of the stresses at maximal load; c. Bar plot of the Young's moduli (one-way Anova analysis: no statistically significant differences; $P > 0.05$).

statistically the same before ($P = 89.28 \pm 2.38$ %) and after Ar DBD ($P = 90.46 \pm 1.49$ %) and Ar PJ ($P = 88.07 \pm 1.48$ %) treatments. In previous studies, electrospun PCL fibers showed signs of melted joining points and more drastic morphological deterioration when subjected to the same Ar and air DBD treatments respectively [26]. This highlights again the enhanced mechanical and thermal properties of PA fibers compared to other polyester fibers.

3.5. *Tensile testing pre- and post-plasma treatments*

Next to the importance of the topographical and surface chemical properties of NGCs, it is imperative that their mechanical properties match the soft nature of the peripheral nerves within certain acceptable limits. In fact, if the NGC is too soft, the surgical implantation becomes very challenging and the risk of collapse in vivo increases. However, if too rigid, the NGC can exert an unwanted chronic compression on the regenerating nerve [18]. Therefore, in order to assess the mechanical suitability of the designed NGCs and examine whether the different plasma treatments were altering their mechanical performance, the typical stress-strain curves of all NGCs were recorded under tensile loading. The ultimate stress at maximal load and the Young's modulus were then obtained with values equal to 2.2 MPa and 8.0 MPa for the untreated NGCs respectively (Fig. 5 B). Interestingly, the acquired ultimate stress closely matched the one of a rat sciatic nerve being 2.7 MPa

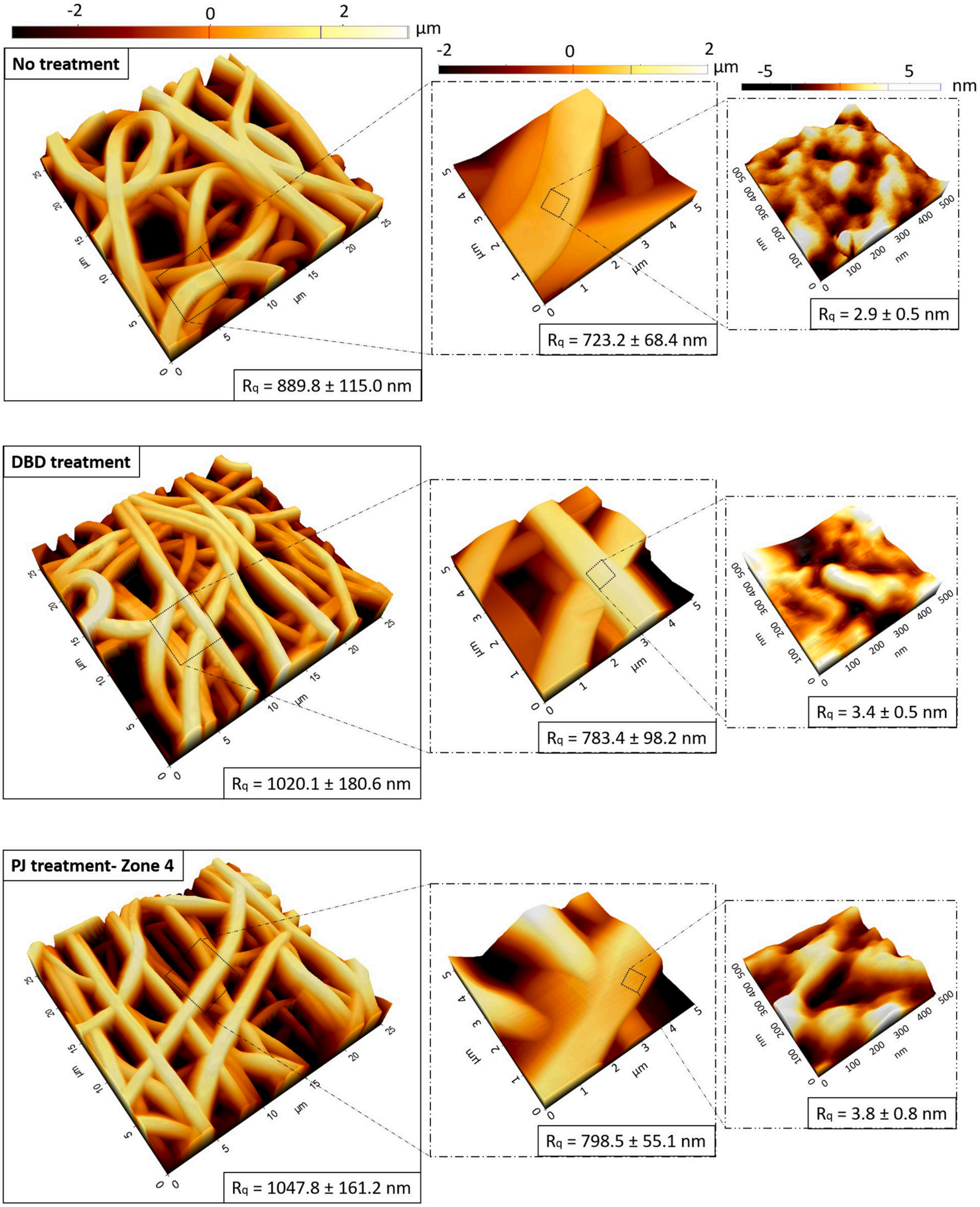

Fig. 6. AFM images of the inner NGC wall pre- and post-plasma treatments (scan sizes: 25 × 25 μm^2; 5 × 5 μm^2 and 500 × 500 nm^2).

as was assessed by Borschel at al [19]. Moreover, Santos et al. have also detected a comparable mechanical performance (Tensile stress: 2.6 MPa and Young's modulus: 10.5 MPa) of electrospun PA NGCs made up of the same ratio of PEOT (55) to PBT (45). Despite their relatively thin wall and high porosity, such NGCs had a slow degradation rate without any sign of collapse for at least 4 months post-implantation in rats thus offering a long-term support for the slow regeneration in long nerve defects [4]. In fact, when comparing the obtained results with the mechanical properties of other NGCs made up of conventional synthetic and natural polymers, one can notice the enhanced flexibility and resilience of PA NGCs. For instance, Prabhakaran et al. have shown that electrospun PCL, chitosan and PCL/chitosan exhibited considerably higher Young's modulus values reaching 35, 28 and 65 MPa respectively. Moreover, lower tensile strengths in the range of 0.22–1.31 MPa were detected thus deviating more from the strength of the native nerve [20]. Luckily, the different plasma treatments were revealed not to alter the desirable mechanical properties of the electrospun PA NGCs. The average values of the ultimate stress and Young's modulus after Ar DBD, air DBD and Ar PJ treatments were 2.1, 2.2 & 2.2 MPa and 9.3, 9.5 & 8.0 MPa respectively (Fig. 5 B). The statistical analysis showed no significant differences pre- and post-plasma treatments. Ar DBD treatment, which produces a homogeneous surface oxygen incorporation, and Ar PJ treatment, which creates a surface oxygen gradient, were the only two conditions considered for the following AFM and in vitro characterization.

3.6. Surface roughness pre- and post-plasma treatments

Since cell performances can be greatly influenced by the underlying surface roughness of the material on which they are adhering/growing, AFM measurements were performed on the 4 zones of the inner NGC wall to determine its roughness pre- and post-plasma treatment. Given the fact that all zones of every NGC condition exhibited similar fiber morphology and Rq values, the results of zone 4 are only presented. Fig. 6 shows the recorded high-resolution AFM images narrowed down from a scanning area of 25 × 25 μm^2 to areas of 5 × 5 μm^2 and 500 × 500 nm^2 with the corresponding Rq values. This progressively scaled down strategy was followed to ultimately image and assess the roughness of a single nanofiber. In this way, one can detect with a very high precision if the different plasma treatments have caused any changes in the surface roughness of the NGCs. This high precision was purposely looked for since neurons and SCs were revealed to sense nanoscale roughness with a high sensitivity to variations of only a few nanometers [72,73]. All images revealed that the nanofibers displayed a homogeneous cylindrical structure across their length but appeared wider than their real diameter because of the geometry of the used AFM tip. Rq values of 890 nm and 723 nm were perceived on the inner nanofibrous mesh of the untreated NGCs as measured on the AFM images having scanning areas of 25 × 25 μm^2 and 5 × 5 μm^2 respectively. A relatively smooth surface of individual fibers was spotted given the obtained low Rq value of 3 nm. The exposure of the fibers to argon DBD and PJ did not cause any variations in their surface roughness as the obtained Rq values indicated no statistical differences. The AFM images of the 4 zones of the PJ-treated NGCs are shown in the supporting information (Fig. S2).

3.7. Comparative in vitro SC study on untreated and plasma-treated NGCs

The ultimate goal of implementing plasma-induced chemical features on the surface of NGCs was to promote glial cell performances for an enhanced nerve regeneration across critical defects. Therefore, the final step of this paper was to assess the bioresponsive properties of untreated and plasma-modified NGCs through a comparative in vitro study using primary SCs.

3.7.1. SCs-surface interactions along the NGCs

Since SCs are the primary glial cells of the peripheral nervous system playing a key role in nerve regeneration, they should adhere, proliferate and migrate effectively on the NGCs [37]. In order to visualize the interaction of SCs with the complete untreated, homogeneously treated and gradient NGC surfaces, 12 overlapping immunofluorescent images were acquired along the inner wall and stitched together. Fig. 7A shows the final fluorescent images of SCs cultured on the different NGCs in the presence of FBS for 1, 3 and 7 days. Moreover, in order to quantify and more precisely sense the cell distribution along the NGCs, fluorescent intensity curves were plotted as a function of the position on the NGC (Fig. S4). To better compare between the different NGC zones and NGC conditions the average fluorescent intensity of every zone of all NGCs was calculated and plotted (Fig. 7B). Regardless of the culturing day, untreated NGCs showed a drastically lower cell density illustrated by a significantly lower overall fluorescent intensity compared to plasma-treated NGCs. A more or less constant fluorescent intensity and therefore a uniform cell distribution was observed along the homogeneously plasma-treated NGCs as no statistically significant difference between the average fluorescent densities of the 4 zones was detected. However, cell gradients towards increased surface oxygen contents were interestingly visualized on the NGCs subjected to a gradient plasma treatment. This was further corroborated by the gradually increasing fluorescent intensity values along the NGCs. These clear variations in cytocompatibility on the different NGCs highlighted the importance of plasma-induced oxygen-containing functionalities and subsequent enhanced wettability in enhancing cellular behaviors starting from the initial attachment. In fact, hydroxyl, carbonyl and carboxyl groups were previously shown to steadily bind proteins without affecting their natural conformation [22,74]. The immobilized proteins serve as recognition sites for cell receptors of which the integrin family playing a key role in the primary cell capture efficiency and cell attachment via the formation of focal adhesion complexes at the contact surface [26,45]. Since the surface of untreated NGCs contained considerably less polar groups and therefore less bioactive sites for protein adsorption, fewer receptors per cell end up attaching to the surface thus engendering small cell/surface contact areas. However, plasma-induced surface oxygen groups acted as glue fastening proteins on the surface thus recruiting a significantly increased number of cell receptors binding to the surface. This results in: 1) an enhanced adhesion of cells that firmly attached to and stretched out on the NGC surface and/or 2) an increased number of adhering cells. Since DNA assay results (Supporting information S2.3) revealed statistically unchanged DNA concentrations on untreated and plasma-treated NGCs at day 1 and 3 post-cell seeding, one can therefore conclude that the increased fluorescent intensity on treated NGCs was mainly due to a better cell adhesion (larger fluorescent cell areas) rather than higher cell numbers. Prabhakaran et al. have also perceived a considerably upgraded SC adhesion on air plasma-treated PCL nanofibers compared to their untreated counterpart but also to PCL/collagen fibers, thus particularly pointing out the notable importance of plasma-induced oxygen functionalities [32]. At day 7 post-SC seeding, the heightened fluorescent intensity on plasma-treated NGCs could be also attributed to an enhanced cell proliferation. This is actually elucidated by the obtained Presto blue® and DNA assay results that indicated considerably higher metabolic activity and cell number on plasma-treated NGCs respectively (Supporting information S2.3). Actually, the formation of robust focal adhesion complexes on plasma-treated surfaces leads to the phosphorylation of a focal adhesion kinase triggering several signal transduction pathways responsible for cell survival, proliferation and other vital cell functions [21,74]. However, the diminished level of initial cell adhesion on untreated NGCs hampered the proper occurrence of subsequent cellular activities thus preventing cell proliferation as revealed by the statistically unchanged DNA concentration over the days. Several previous studies have indeed proven that plasma-incorporated oxygen-containing functionalities enhanced cell growth and proliferation in addition to their crucial role in promoting

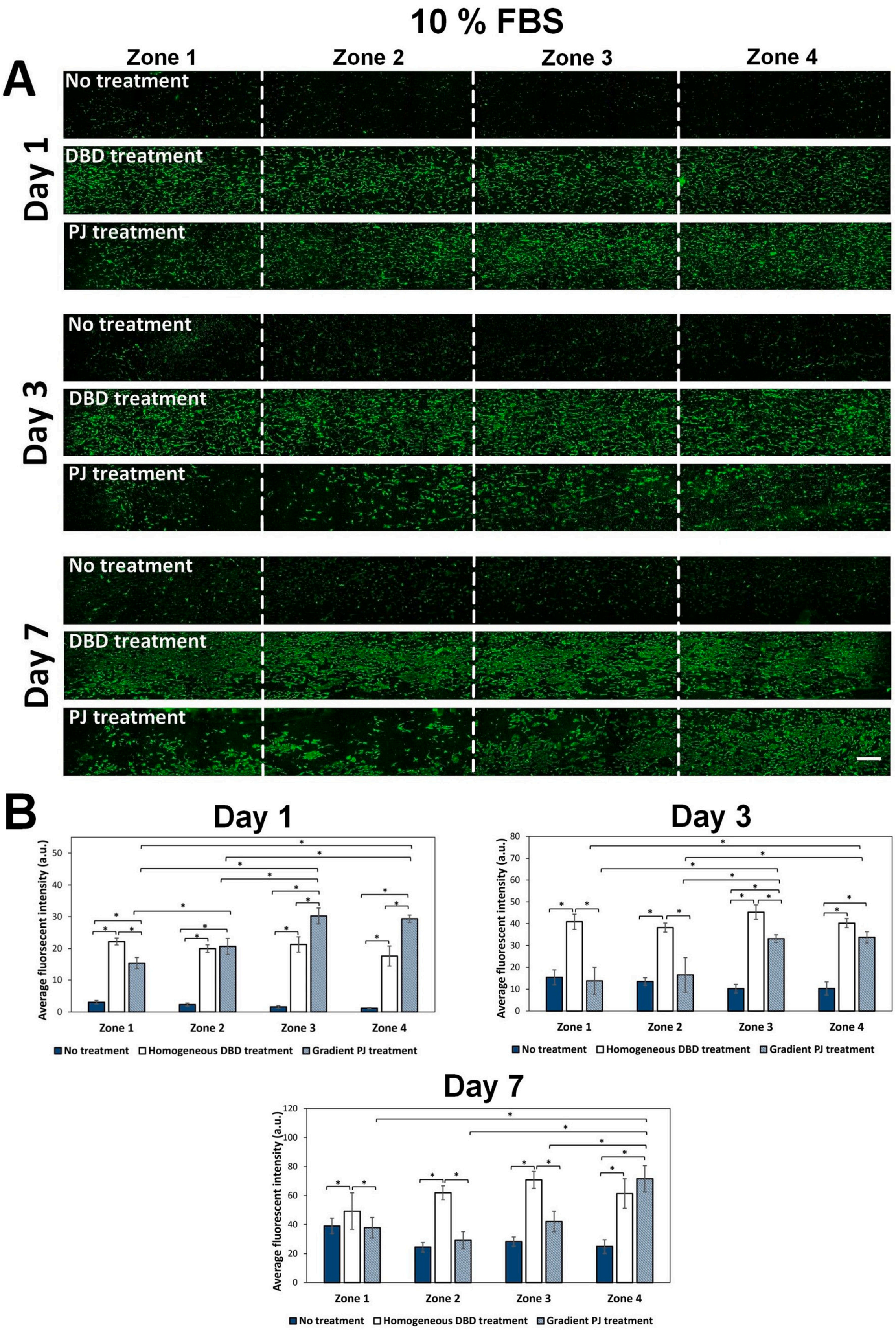

Fig. 7. A) S100 immunofluorescent images of SCs on the full NGC length after 1, 3 and 7 days of culturing in the presence of 10 % FBS (scale bar: 1000 μm). B) Bar plots of the corresponding average fluorescent intensity in the NGC zones (*: statistically significant difference P < 0.05).

cell adhesion [21,22,24,31,32]. Since a gradient distribution of oxygen groups was detected on PJ treated NGCs, protein adsorption increased gradually along this gradient, proportionally recruiting integrins and anchoring more and more focal adhesive complexes along the NGCs. This can explain how the density and/or area of SCs attached on the surface intensifies in parallel with the oxygen gradient. Since the surface roughness of the overall inner nanofibrous wall and its individual nanofibers did not change post-plasma treatments, one can be sure that the surface chemistry is solely behind the improved cell-material interactions.

SCs were also cultured on the NGCs without the direct presence of FBS in the medium in order to elucidate whether they could sense similarly or differently the plasma-induced surface changes. Fig. 8 portrays again the corresponding immunofluorescent images and average fluorescent intensity bar plots of each NGC zone acquired at day 1, 3 and 7 of culturing. Cell adhesion occurring in an FBS-free medium was due to the prior adsorption of proteins on the NGCs during their immersion in FBS the night before cell seeding. Therefore, similar trends were detected on untreated versus plasma-treated NGCs as compared to the first set of in vitro tests in which FBS was present in the culturing medium. Nonetheless, regardless of the surface treatment, a higher overall fluorescent intensity was clearly visualized in the presence of FBS. This is due to the fact that proteins present in the serum continued to attach to the surface during cell culturing, anchoring more focal adhesion complexes and therefore further enhancing cell adhesion. A stagnation in the metabolic activity and DNA concentration was observed over the culturing days when an FBS-free medium was used (Supporting information S2.3). This suggests that the pre-adsorbed FBS proteins on the NGCs were not enough to maintain adequate cell growth and division. The extra direct interactions between cells and proteins provided by the FBS present in the medium were therefore essential for long term cell performances.

When taking a closer look at the PJ-treated NGCs, some differences in the cell gradient distribution could be visualized at different culturing days on the one hand and in the presence or absence of FBS on the other hand. At day 1, the cell gradient was less pronounced when FBS was present in the medium. In fact, when FBS is present, statistically significant differences in the average fluorescent intensities were detected between zone 1 and zones 2, 3 and 4 and between zone 2 and zone 4 but not between zone 3 and zone 4. In the absence of FBS, statistically significant difference was additionally observed between zone 3 and zone 4. This is presumably attributed to the extra amount of adsorbed proteins on the complete NGC in the presence of FBS, reducing the cell receptor ability to sense small differences in spatial ligand concentrations in the last 2 zones. The optimal amount of adsorbed proteins seemed to be already reached somewhere on the intermediate zones (Fig. 7).

At day 3, the cell gradient in the presence of FBS became more prominent, while the cell gradient in the absence of FBS became considerably less pronounced when comparing to day 1. Statistically significant difference in the average fluorescent intensity is only observed between zone 1 and 3 when FBS is absent. In fact, after initial attachment, cells normally enter the lag-stage in which an adaptation to the surrounding microenvironment occurs [75]. The absence of FBS probably led to the perturbation of the cells in the lag-stage causing the partial loss of the gradient cell dispersion. In contrast, in the presence of FBS, cells most likely underwent the lag-stage more smoothly and rapidly. The steeper cell gradient illustrated by higher fluorescent intensities on zone 3 and 4 could be produced by 2 mechanisms: 1) a higher proliferation on the oxygen-rich end as a response to the better prior adhesion; 2) a directed cell migration towards higher surface oxygen content, hence higher adsorbed protein concentration. Nonetheless, since the same DNA concentration was detected on the NGCs at days 1 and 3, one can conclude that the cell migration was mainly causing this pronounced gradient and not the cell proliferation. Some authors have indeed shown that cells tend to polarize unidirectionality on chemical gradients by redistributing their chemosensory signaling receptors and organelles towards higher ligand density side [36,76,77]. For instance, Warneken et al. and Arnold et al. have modulated the spatial distribution of integrins on the cell membrane leading to cell polarization after the implementation of defined surface peptide gradients [78,79]. When the polarization persists in a unique direction owing to permanent gradient signaling, a contraction of cytoskeletal filaments pulls the cellular body towards the leading edge and cell migration occurs in succession. Moreover, cells on chemical gradients tend to attach more tightly at one end. The resulting imbalance in the adhesive forces can lead to the movement in the direction of the boosted adhesiveness [36,76]. Motta et al. have studied the migration of SCs on micro-engineered glass substrates tethered with laminin-derived peptide gradients and revealed that YIGSR peptide gradients directed SC migration but not RGD gradients [36]. Therefore, the simple plasma-induced oxygen gradient was shown to surpass some immobilized peptide gradients in stimulating SC chemotaxis.

At day 7, an inverse gradient steepness is again detected. The cell gradient in the absence of FBS became more protruding when comparing to day 3 (Fig. 8). In fact, the average fluorescent intensities of zones 1, 2 and 3 were statistically lower than that of zone 4. This is presumably associated with one or both of the following assumptions: 1) the cells on the low oxygen content zones did not manage to survive while more cells on the rich-oxygen end stayed alive given their initial stronger adhesion and the presence of more proteins, 2) the surviving cells underwent a directional migration that was further facilitated by the initial lower adhesive forces compared to the tighter adhesion occurring in the presence of FBS. The cellular gradient was still clearly perceived in the presence of FBS where cells started to fully cover the oxygen-rich extremity not leaving space for more cells to attach. The average fluorescent intensity of zone 4 doubled when comparing to day 3. This was associated with an enhanced cell proliferation at the oxygen-rich end accompanying cell chemotaxis, since the DNA concentration significantly increased at day 7 compared to day 3. Therefore, a lateral accumulation of the proliferating and migrating cells started to be noticed on the intermediate zones.

3.7.2. Morphological studies of SCs on different zones of the NGCs

In addition to enhanced cell adhesion, proliferation and migration, SC morphology and directionality are two extra parameters playing a leading role in neurogenesis [37,80]. Therefore, individual S100 immunostaining images of higher magnification were also acquired to closely visualize SCs cultured for 3 days without and with FBS on untreated and plasma-treated NGCs (Figs. 9A and 10A). Fluorescent images of SCs cultured on the tissue culture plate (positive control) are shown in the supporting information (Fig. S5). ##The fluorescent images were complemented with SEM images for a more detailed scrutiny on how the cells were attached and shaped on the PA fibers (Figs. 9B and 10 B). A zone-specific analysis was only performed for PJ treated samples since untreated and DBD treated NGCs exhibited the same SC morphology and orientation over their full length. An arbitrary image of one of the 4 zones is therefore only shown in case of untreated and homogeneously treated NGCs. Regardless of the presence and absence of FBS in the culture medium, SCs cultured on untreated NGCs remained rounded with very tiny body areas in close contact with PA fibers, thus indicating a poor cell adhesion. However, planar and completely spread out SCs were observed on plasma-treated NGCs: the homogeneous DBD treatment showed a relatively equal combination of star-like and spindle-shaped SCs while the PJ gradient treatment displayed different cell morphologies along the 4 zones. A higher occurrence of star-like and multi-polar radially spread out SCs were visualized on low oxygen content areas (zone 1). A gradual change to spindle-shaped bipolar morphologies befell towards areas of increasing oxygen contents. Zone 4 showed therefore a higher incidence of aligned cells stretching out unidirectionally and overextending on longer distances. This qualitative visualization of different cell morphologies was quantitatively

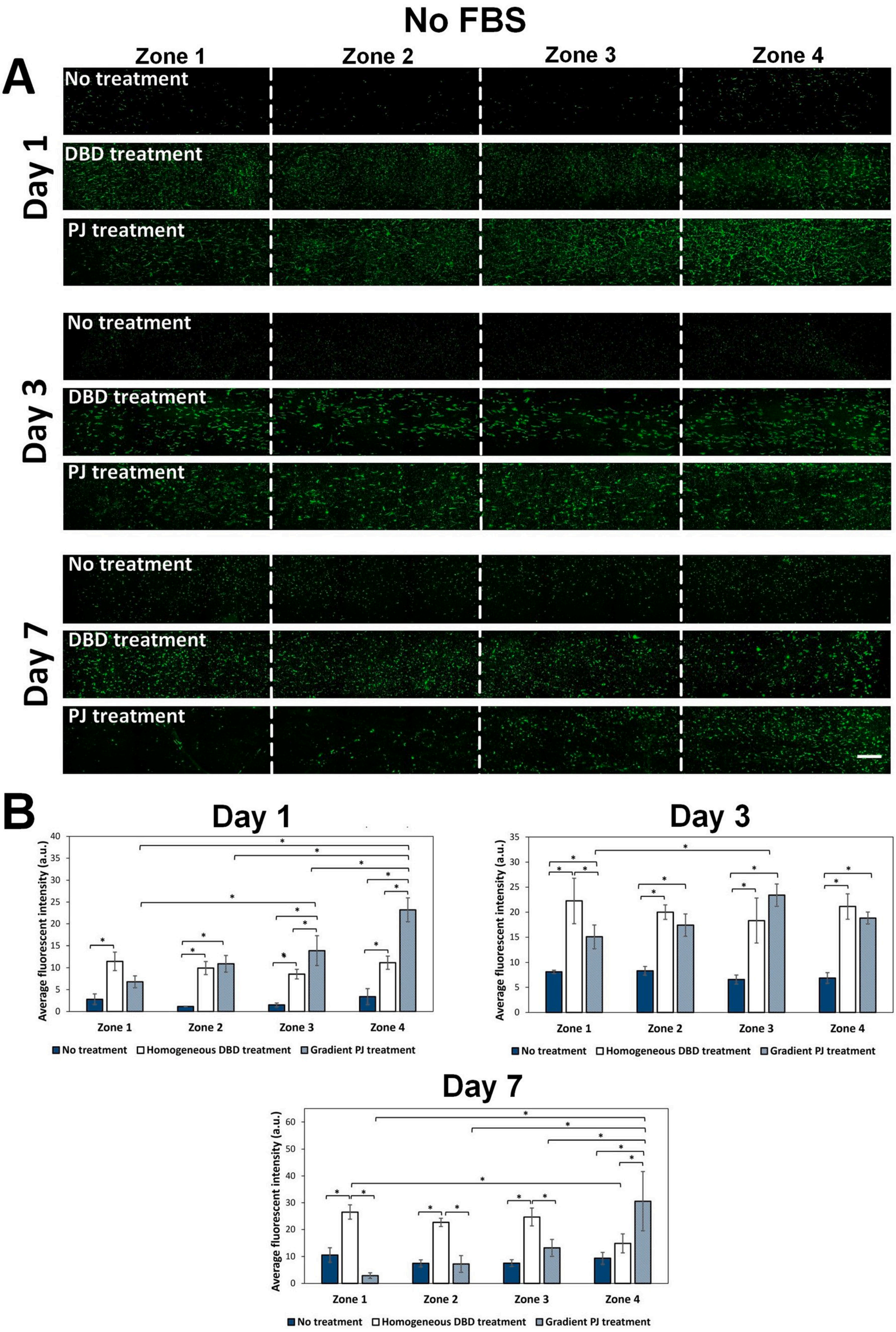

Fig. 8. A) S100 immunofluorescent images of SCs on the full NGC length after 1, 3 and 7 days of culturing in the absence of FBS (scale bar: 1000 μm). B) Bar plots of the corresponding average fluorescent intensity in the NGC zones (*: statistically significant difference $P < 0.05$).

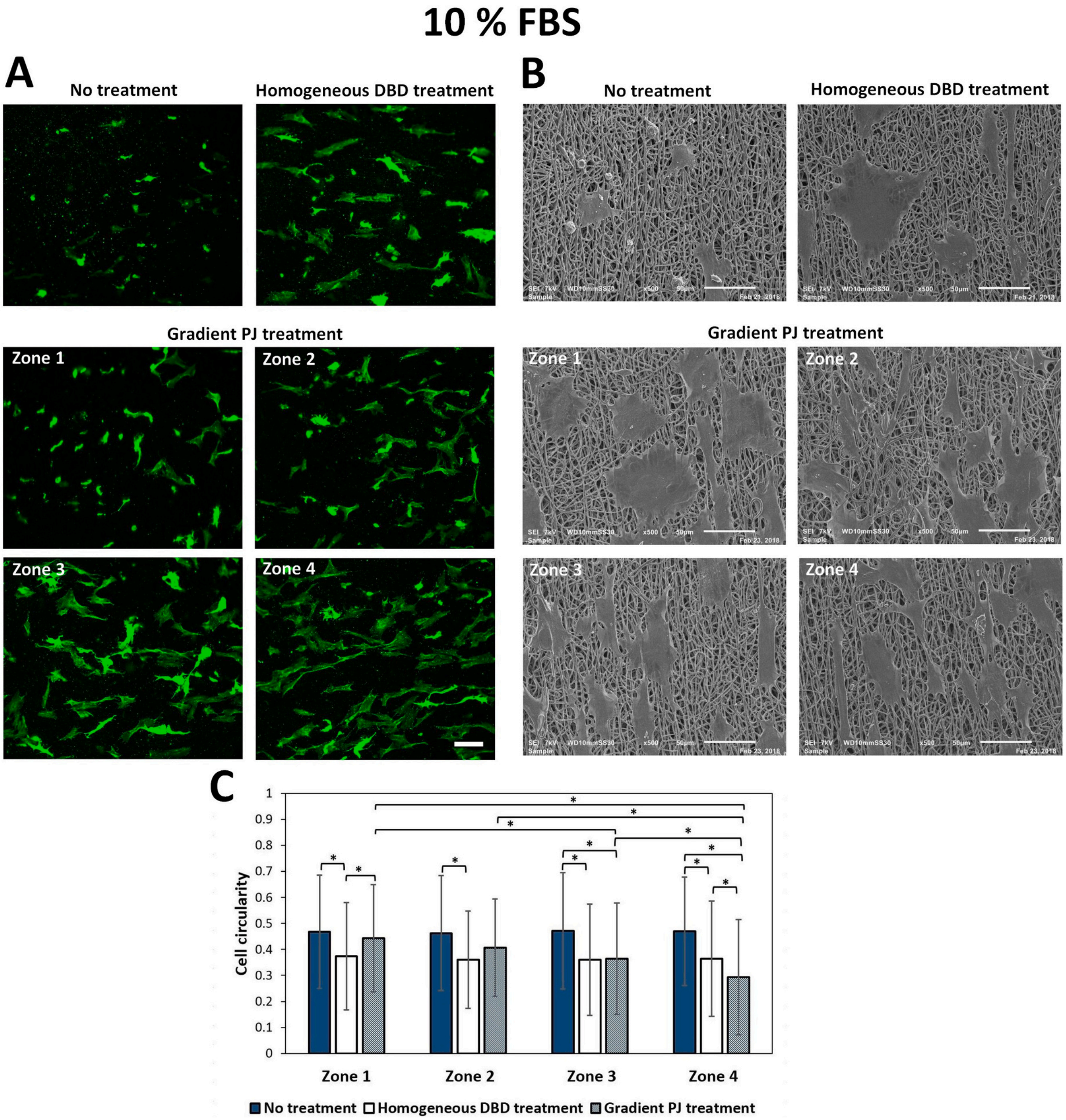

Fig. 9. S100 immunofluorescent images (A; scale bar: 100 μm) and SEM images (B; scale bar: 50 μm) of SCs cultured for 3 days on untreated, DBD treated and 4 zones of PJ treated NGCs in the presence of 10 % FBS. C) Corresponding SC circularity values on the 4 zones of untreated, DBD treated and PJ treated NGCs (*: statistically significant difference $P < 0.05$).

confirmed by measuring the cell circularity on the 4 zones of the differently treated NGCs (Figs. 9C and 10C). In all cases, a higher value of cell circularity was detected on untreated NGCs which is an indication of more circular cells compared to the more elongated cells present on plasma-treated NGCs. In fact, the rare focal adhesive complexes that succeeded to form on untreated NGCs probably consisted of few anchor points leading to scarcely attached rounded cells. However, plasma-treated NGCs attracted more proteins to adsorb on their oxygen-rich surface leading to the creation of numerous focal adhesion sites with stable anchor points spreading out the cells on the surface. Many other cell types were previously shown to adopt similar morphologies on untreated versus plasma-treated electrospun fibers [21,22,81,82]. Both spindle-shaped and star-like morphologies adopted by SCs when spreading on plasma-treated NGCs could be linked back to the inner wall architecture made up of alternating bundles of aligned fibers and random fibers respectively. In fact, focal adhesion complexes were dispersed arbitrarily on the overlapping multidirectional random fibers ending up by the attachment of multipolar cells. However, aligned fibers are known to have a great ability in providing contact guidance aligning the cells. On the one hand, this is due to the aligned positioning of focal complexes on parallel fibers. On the other hand, traction forces are exerted on the cytoskeleton in the aligned fiber direction leading to protrusions and actin polymerization parallel to the fibers [83]. Gupta et al., Masaeli et al. and Idini et al. have indeed shown that SCs grown on aligned fibers exhibit a bipolar morphology oriented along the fiber direction, while SCs seeded on random fibers adopt a multipolar morphology [9,37,46]. The extra gradual elongation and orientation of cells perceived along PJ treated NGCs was driven by the oxygen gradient. MC3T3 osteoblasts were also seen to gradually change from a more circular shape to a more elongated shape along a peptide gradient [78,79]. This is due, as already mentioned, to the redistribution of the chemosensory receptors towards the high protein density end,

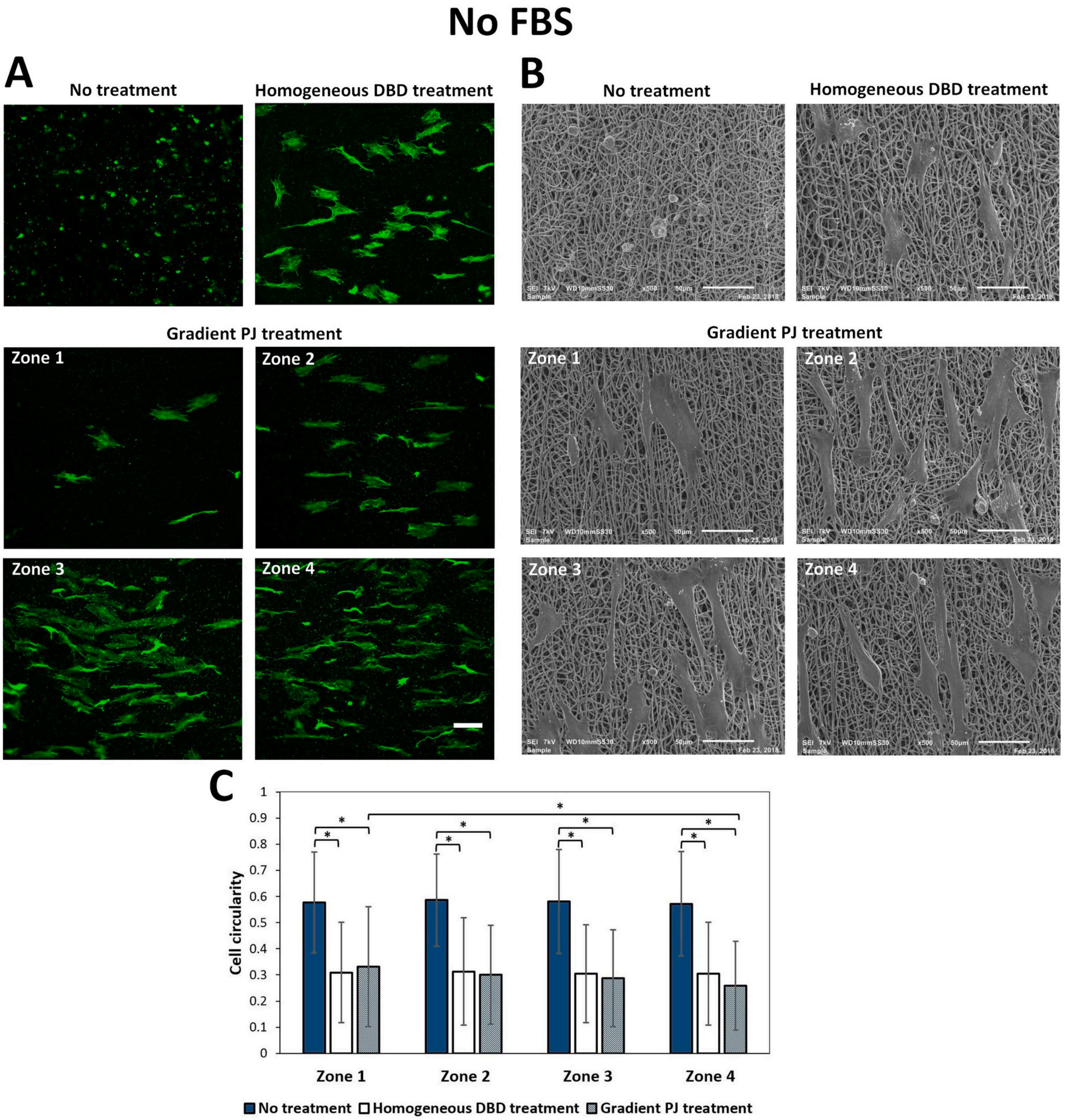

Fig. 10. S100 immunofluorescent images (A; scale bar: 100 μm) and SEM images (B; scale bar: 50 μm) of SCs cultured for 3 days on untreated, DBD treated and 4 zones of PJ treated NGCs in the absence of FBS. C) Corresponding SC circularity values on the 4 zones of untreated, DBD treated and PJ treated NGCs (*: statistically significant difference $P < 0.05$).

polarizing and aligning the cells. The synergistic influence of the aligned underlying fibers and the surface oxygen gradient accentuated the formation of SC columns mimicking the bands of Büngner formed during nerve regeneration. In fact, the bands of Büngner are composed of unidirectionally elongated SCs that selectively guide regrowing axons [37,80]. The presumed mechanism underlying their formation is the polarized expression of specific adhesion proteins on the SC axis, which is close to what takes place on gradient surfaces [84].

When comparing SCs cultured with and without FBS, some differences in cell morphology and circularity could also be clearly perceived. In addition to the 3D ball-shaped cells observed on untreated NGCs in the absence of FBS, some star-like cells will small cell bodies were also attached when FBS was used. This was affirmed by the slightly lower averaged cell circularity value in presence of FBS. This was again due to the occurrence of more bioactive sites created by the extra proteins present in the FBS. In case of PJ treated NGCs, the elongation of SCs along the oxygen gradient was more pronounced when FBS is absent. Almost all cells became very elongated reaching a fibrous-like morphology on zone 4. Whereas, when FBS was present, few multipolar and disoriented cells could still be observed on zone 4. This is presumably due to the lower spacing between adsorbed proteins on the NGC in the presence of FBS, reducing the cell ability to sense the differences between its back and front and therefore to better orient itself in the gradient direction. In fact, few authors have revealed that cells elongate themselves along gradient surfaces when the average distance between ligands is larger than a certain non-detectable small spacing [78,79]. Nonetheless, when taking a look at the overall cell circularity values, one can notice that statistically different values were only detected between zone 1 and 4 in the absence of FBS. More gradual and statistically significant changes in the cell circularity were detected in between the 4 zones in the presence of FBS.

Finally, PC12 cells were cultured on SC pre-seeded NGCs to test their potential in triggering neurite extension as a proof of concept. Neurite outgrowth was only detected on plasma-treated NGCs: DBD treated NGCs displayed relatively short neurites extending in multiple directions, while PJ treated NGCs showed gradually longer neurites mainly directed towards higher oxygen contents (Supporting information S2.6).

4. Conclusion

In the present study, PA NGCs were electrospun using fine-tuned process parameters producing an inner wall comprised of bundles of aligned fibers with random fibers in between and an outer wall fully composed of random fibers. The double-layered architecture was conceived in a simple one-step process to synergistically provide directional cues guiding neurite extension and triggering SC elongation while allowing a sufficient nutrient supply. The NGCs were then subjected to different plasma treatments to promote the inner surface chemical properties for improved SC performances. Medium pressure Ar DBD treatment homogeneously increased the surface oxygen content from 17 % to 28 %, thus highlighting the plasma ability to penetrate through the porous wall. Atmospheric pressure Ar PJ treatment created a gradient chemistry throughout the inner wall with an oxygen content gradually increasing from 21 % to 30 %. No fiber morphological and surface roughness variations or mechanical deterioration were detected post-plasma treatments. Enhanced SC-surface interactions were observed on plasma-treated NGCs compared to their untreated counterparts. A uniform cell distribution was visualized along the homogeneously plasma-treated NGCs. However, cell gradients towards increased surface oxygen contents were interestingly detected on the NGCs subjected to a gradient plasma treatment. With time, the cell gradient became steeper and more prominent owing mainly to a directed cell migration along the NGCs and to a better cell proliferation on the oxygen-rich end. SCs cultured on untreated NGCs remained rounded while planar and completely spread out SCs were observed on plasma-treated NGCs. A gradual change from a more circular shape to a more elongated shape was perceived along the oxygen gradient thus forming SC columns mimicking the natural bands of Büngner structure. Overall, it can be concluded that plasma-treated PA NGCs have a great potential in nerve tissue engineering applications. Particularly, a plasma-induced chemistry gradient along the inner wall is believed to strongly enhance a directed and far-reaching nerve regeneration, thus paving the way towards critical nerve gap repair. A future translation from in vitro to in vivo tests will hopefully constitute a big step towards the clinical use of the conceived NGCs.

CRediT authorship contribution statement

Rouba Ghobeira: Conceptualization, Data curation, Formal analysis, Investigation, Methodology, Software, Funding acquisition, Writing – original draft. **Paul Wieringa:** Conceptualization, Supervision, Validation. **Stijn Van Vrekhem:** Formal analysis. **Sheida Aliakbarshirazi:** Investigation. **Mehrnoush Narimisa:** Investigation. **Iuliia Onyshchenko:** Investigation. **Nathalie De Geyter:** Conceptualization, Funding acquisition, Project administration, Resources, Validation, Writing – review & editing. **Lorenzo Moroni:** Conceptualization, Validation, Resources, Visualization, Writing – review & editing. **Rino Morent:** Conceptualization, Project administration, Resources, Supervision, Validation, Visualization, Writing – review & editing.

Declaration of competing interest

The authors of the manuscript declare that there are no conflicts of interest.

Data availability

The authors are unable or have chosen not to specify which data has been used.

Acknowledgments

R. Ghobeira would like to thank the Research Foundation Flanders-Belgium (FWO-grant number 12ZC720N) for financing her post-doctoral position. R. Ghobeira also received funding from the FWO (V430617N) for a scientific stay at Maastricht University - MERLN institute. S. Aliakbarshirazi would like to acknowledge the support of the Special Research Fund (BOF.24Y.2017.0003.01) of Ghent University.

Appendix A. Supplementary data

Supplementary data to this article can be found online at https://doi.org/10.1016/j.bioadv.2022.213183.

References

[1] J. Wang, W. Zheng, L. Chen, T. Zhu, W. Shen, C. Fan, H. Wang, X. Mo, Enhancement of Schwann cells function using graphene-oxide-modified nanofiber scaffolds for peripheral nerve regeneration, ACS Biomater Sci. Eng. 5 (5) (2019) 2444–2456.

[2] J. Xie, M.R. MacEwan, W. Liu, N. Jesuraj, X. Li, D. Hunter, Y. Xia, Nerve guidance conduits based on double-layered scaffolds of electrospun nanofibers for repairing the peripheral nervous system, ACS Appl. Mater. Interfaces 6 (12) (2014) 9472–9480.

[3] W. Daly, L. Yao, D. Zeugolis, A. Windebank, A. Pandit, A biomaterials approach to peripheral nerve regeneration: bridging the peripheral nerve gap and enhancing functional recovery, J. R. Soc. Interface 9 (67) (2012) 202–221.

[4] D. Santos, P. Wieringa, L. Moroni, X. Navarro, J.D. Valle, Peot/Pbt guides enhance nerve regeneration in long gap defects, Adv. Healthc. Mater. 6 (3) (2017), 1600298.

[5] L. Zhu, S. Jia, T. Liu, L. Yan, D. Huang, Z. Wang, S. Chen, Z. Zhang, W. Zeng, Y. Zhang, Aligned pcl fiber conduits immobilized with nerve growth factor gradients enhance and direct sciatic nerve regeneration, Adv. Funct. Mater. 30 (39) (2020), 2002610.

[6] R. Deumens, A. Bozkurt, M.F. Meek, M.A. Marcus, E.A. Joosten, J. Weis, G. A. Brook, Repairing injured peripheral nerves: bridging the gap, Prog. Neurobiol. 92 (3) (2010) 245–276.

[7] X. Jiang, S.H. Lim, H.-Q. Mao, S.Y. Chew, Current applications and future perspectives of artificial nerve conduits, Exp. Neurol. 223 (1) (2010) 86–101.

[8] C.R. De Carvalho, J.M. Oliveira, R.L. Reis, Modern trends for peripheral nerve repair and regeneration: beyond the hollow nerve guidance conduit, Front. Bioeng. Biotechnol. 7 (2019) 337.

[9] M. Idini, P. Wieringa, S. Rocchiccioli, G. Nieddu, N. Ucciferri, M. Formato, A. Lepedda, L. Moroni, Glycosaminoglycan functionalization of electrospun scaffolds enhances schwann cell activity, Acta Biomater. 96 (2019) 188–202.

[10] S. Behtaj, J.A. Ekberg, J.A. St John, Advances in electrospun nerve guidance conduits for engineering neural regeneration, Pharmaceutics 14 (2) (2022) 219.

[11] X. Gu, F. Ding, Y. Yang, J. Liu, Construction of tissue engineered nerve grafts and their application in peripheral nerve regeneration, Prog. Neurobiol. 93 (2) (2011) 204–230.

[12] A.M. McGrath, L.N. Novikova, L.N. Novikov, M. Wiberg, Bd™ Puramatrix™ peptide hydrogel seeded with schwann cells for peripheral nerve regeneration, Brain Res. Bull. 83 (5) (2010) 207–213.

[13] G.C. De Ruiter, R.J. Spinner, M.J. Malessy, M.J. Moore, E.J. Sorenson, B.L. Currier, M.J. Yaszemski, A.J. Windebank, Accuracy of motor axon regeneration across autograft, single-lumen, and multichannel poly (Lactic-co-glycolic Acid) nerve tubes, Neurosurgery 63 (1) (2008) 144–155.

[14] Y. Zhu, A. Wang, S. Patel, K. Kurpinski, E. Diao, X. Bao, G. Kwong, W.L. Young, S. Li, Engineering bi-layer nanofibrous conduits for peripheral nerve regeneration, Tissue Eng. Part C Methods 17 (7) (2011) 705–715.

[15] J.I. Kim, T.I. Hwang, L.E. Aguilar, C.H. Park, C.S. Kim, A controlled design of aligned and random nanofibers for 3d bi-functionalized nerve conduits fabricated via a novel electrospinning set-up, Sci. Rep. 6 (1) (2016) 1–12.

[16] A. Subramanian, U.M. Krishnan, S. Sethuraman, Fabrication of uniaxially aligned 3d electrospun scaffolds for neural regeneration, Biomed. Mater. 6 (2) (2011), 025004.

[17] J. Xie, M.R. MacEwan, A.G. Schwartz, Y. Xia, Electrospun nanofibers for neural tissue engineering, Nanoscale 2 (1) (2010) 35–44.

[18] W. Yu, W. Zhao, C. Zhu, X. Zhang, D. Ye, W. Zhang, Y. Zhou, X. Jiang, Z. Zhang, Sciatic nerve regeneration in rats by a promising electrospun collagen/poly (E-Caprolactone) nerve conduit with tailored degradation rate, BMC Neurosci. 12 (1) (2011) 68.

[19] G.H. Borschel, K.F. Kia, W.M. Kuzon Jr., R.G. Dennis, Mechanical properties of acellular peripheral nerve, J. Surg. Res. 114 (2) (2003) 133–139.

[20] M.P. Prabhakaran, J.R. Venugopal, T.T. Chyan, L.B. Hai, C.K. Chan, A.Y. Lim, S. Ramakrishna, Electrospun biocomposite nanofibrous scaffolds for neural tissue engineering, Tissue Eng. A 14 (11) (2008) 1787–1797.

[21] R. Ghobeira, C. Philips, L. Liefooghe, M. Verdonck, M. Asadian, P. Cools, H. Declercq, W.H. De Vos, N. De Geyter, R. Morent, Synergetic effect of electrospun pcl fiber size, orientation and plasma-modified surface chemistry on stem cell behavior, Appl. Surf. Sci. 485 (2019) 204–221.

[22] A. Martins, E.D. Pinho, S. Faria, I. Pashkuleva, A.P. Marques, R.L. Reis, N.M. Neves, Surface modification of electrospun polycaprolactone nanofiber meshes by plasma treatment to enhance biological performance, Small 5 (10) (2009) 1195–1206.

[23] S. Madduri, K. Feldman, T. Tervoort, M. Papaloïzos, B. Gander, Collagen nerve conduits releasing the neurotrophic factors gdnf and ngf, J. Control. Release 143 (2) (2010) 168–174.

[24] P.S.E. Tabaei, M. Asadian, R. Ghobeira, P. Cools, M. Thukkaram, P. G. Derakhshadeh, S. Abednatanzi, P. Van Der Voort, K. Verbeken, C. Vercruysse, Combinatorial effects of coral addition and plasma treatment on the properties of Chitosan/Polyethylene oxide nanofibers intended for bone tissue engineering, Carbohydr. Polym. 117211 (2020).

[25] P. Cools, C. Mota, I. Lorenzo-Moldero, R. Ghobeira, N. De Geyter, L. Moroni, R. Morent, Acrylic acid plasma coated 3d scaffolds for cartilage tissue engineering applications, Sci. Rep. 8 (1) (2018) 1–15.

[26] R. Ghobeira, C. Philips, V. De Naeyer, H. Declercq, P. Cools, N. De Geyter, R. Cornelissen, R. Morent, Comparative study of the surface properties and cytocompatibility of plasma-treated poly-E-caprolactone nanofibers subjected to different sterilization methods, J. Biomed. Nanotechnol. 13 (6) (2017) 699–716.

[27] C.H. Jang, H. Lee, M. Kim, G. Kim, Effect of polycaprolactone/collagen/Hucs microfiber nerve conduit on facial nerve regeneration, Int. J. Biol. Macromol. 93 (2016) 1575–1582.

[28] H.-C. Ni, Z.-Y. Lin, S.-H. Hsu, I.-M. Chiu, The use of air plasma in surface modification of peripheral nerve conduits, Acta Biomater. 6 (6) (2010) 2066–2076.

[29] S.-H. Hsu, W.-C. Kuo, Y.-T. Chen, C.-T. Yen, Y.-F. Chen, K.-S. Chen, W.-C. Huang, H. Cheng, New nerve regeneration strategy combining laminin-coated chitosan conduits and stem cell therapy, Acta Biomater. 9 (5) (2013) 6606–6615.

[30] X.F. Zhang, H.X. Liu, L.S. Ortiz, Z.D. Xiao, N.P. Huang, Laminin-modified and aligned poly (3-hydroxybutyrate-co-3-hydroxyvalerate)/polyethylene oxide nanofibrous nerve conduits promote peripheral nerve regeneration, J. Tissue Eng. Regen. Med. 12 (1) (2018) e627–e636.

[31] M. Asadian, M. Dhaenens, I. Onyshchenko, S. De Waele, H. Declercq, P. Cools, B. Devreese, D. Deforce, R. Morent, N. De Geyter, Plasma functionalization of polycaprolactone nanofibers changes protein interactions with cells, resulting in increased cell viability, ACS Appl. Mater. Interfaces 10 (49) (2018) 41962–41977.

[32] M.P. Prabhakaran, J. Venugopal, C.K. Chan, S. Ramakrishna, Surface modified electrospun nanofibrous scaffolds for nerve tissue engineering, Nanotechnology 19 (45) (2008) 1–8.

[33] S. Tang, J. Zhu, Y. Xu, A.P. Xiang, M.H. Jiang, D. Quan, The effects of gradients of nerve growth factor immobilized pcla scaffolds on neurite outgrowth in vitro and peripheral nerve regeneration in rats, Biomaterials 34 (29) (2013) 7086–7096.

[34] Y.-C. Chang, M.-H. Chen, S.-Y. Liao, H.-C. Wu, C.-H. Kuan, J.-S. Sun, T.-W. Wang, Multichanneled nerve guidance conduit with spatial gradients of neurotrophic factors and oriented nanotopography for repairing the peripheral nervous system, ACS Appl. Mater. Interfaces 9 (43) (2017) 37623–37636.

[35] M.C. Dodla, R.V. Bellamkonda, Differences between the effect of anisotropic and isotropic laminin and nerve growth factor presenting scaffolds on nerve regeneration across long peripheral nerve gaps, Biomaterials 29 (1) (2008) 33–46.

[36] C.M. Motta, K.J. Endres, C. Wesdemiotis, R.K. Willits, M.L. Becker, Enhancing schwann cell migration using concentration gradients of laminin-derived peptides, Biomaterials 218 (2019), 119335.

[37] E. Masaeli, M. Morshed, M.H. Nasr-Esfahani, S. Sadri, J. Hilderink, A. van Apeldoorn, C.A. van Blitterswijk, L. Moroni, Fabrication, characterization and cellular compatibility of poly (hydroxy alkanoate) composite nanofibrous scaffolds for nerve tissue engineering, PloS one 8 (2) (2013), e57157.

[38] T. Ren, S. Yu, Z. Mao, C. Gao, A complementary density gradient of zwitterionic polymer brushes and ncam peptides for selectively controlling directional migration of schwann cells, Biomaterials 56 (2015) 58–67.

[39] R. Ghobeira, C. Philips, H. Declercq, P. Cools, N. De Geyter, R. Cornelissen, R. Morent, Effects of different sterilization methods on the physico-chemical and bioresponsive properties of plasma-treated polycaprolactone films, Biomed. Mater. 12 (1) (2017), 015017.

[40] I. Onyshchenko, N. De Geyter, A.Y. Nikiforov, R. Morent, Atmospheric pressure plasma penetration inside flexible polymeric tubes, Plasma Process. Polym. 12 (3) (2015) 271–284.

[41] A. El-Fiqi, J.-H. Park, Novel large-volume and highly porous scaffold of poly (E-caprolactone) microfibers/collagen nanofibers for regenerative medicine, Mater. Lett. 322 (2022), 132474.

[42] A. Sadeghi, M. Zandi, M. Pezeshki-Modaress, S. Rajabi, Tough, hybrid chondroitin sulfate nanofibers as a promising scaffold for skin tissue engineering, Int. J. Biol. Macromol. 132 (2019) 63–75.

[43] R. Kaewkhaw, A.M. Scutt, J.W. Haycock, Integrated culture and purification of rat schwann cells from freshly isolated adult tissue, Nat. Protoc. 7 (11) (2012) 1996.

[44] H.B. Wang, M.E. Mullins, J.M. Cregg, C.W. McCarthy, R.J. Gilbert, Varying the diameter of aligned electrospun fibers alters neurite outgrowth and schwann cell migration, Acta Biomater. 6 (8) (2010) 2970–2978.

[45] S. Gnavi, B.E. Fornasari, C. Tonda-Turo, G. Ciardelli, M. Zanetti, S. Geuna, I. Perroteau, The influence of electrospun fibre size on schwann cell behaviour and axonal outgrowth, Mater. Sci. Eng. C 48 (2015) 620–631.

[46] D. Gupta, J. Venugopal, M.P. Prabhakaran, V.G. Dev, S. Low, A.T. Choon, S. Ramakrishna, Aligned and random nanofibrous substrate for the in vitro culture of schwann cells for neural tissue engineering, Acta Biomater. 5 (7) (2009) 2560–2569.

[47] C. Liu, B. Li, X. Mao, Q. Zhang, R. Sun, R.H. Gong, F. Zhou, Controllable aligned nanofiber hybrid yarns with enhanced bioproperties for tissue engineering, Macromol. Mater. Eng. 304 (7) (2019), 1900089.

[48] T. Bini, S. Gao, S. Wang, A. Lim, L.B. Hai, S. Ramakrishna, Electrospun poly (L-lactide-co-glycolide) biodegradable polymer nanofibre tubes for peripheral nerve regeneration, Nanotechnology 15 (11) (2004) 1459.

[49] N. De Geyter, R. Morent, C. Leys, Penetration of a dielectric barrier discharge plasma into textile structures at medium pressure, Plasma Sources Sci. Technol. 15 (1) (2006) 78.

[50] H. Poll, U. Schladitz, S. Schreiter, Penetration of plasma effects into textile structures, Surf. Coat. Technol. 142 (2001) 489–493.

[51] T. Jacobs, N. De Geyter, R. Morent, T. Desmet, P. Dubruel, C. Leys, Plasma treatment of polycaprolactone at medium pressure, Surf. Coat. Technol. 205 (2011) S543–S547.

[52] P. Cools, M. Asadian, W. Nicolaus, H. Declercq, R. Morent, N. De Geyter, Surface treatment of Peot/Pbt (55/45) with a dielectric barrier discharge in air, helium, argon and nitrogen at medium pressure, Materials 11 (3) (2018) 391.

[53] D.M.S. El-Zeer, A. A, U.M. Rashed, T.A. Abd-Elbaset, S. Ghalab, A comparative study between the filamentary and glow modes of Dbd plasma in the treatment of wool fibers, J. Eng. Res. Appl. 4 (3) (2014) 401–410.

[54] J. Jarrige, M. Laroussi, E. Karakas, Formation and dynamics of plasma bullets in a non-thermal plasma jet: influence of the high-voltage parameters on the plume characteristics, Plasma Sources Sci. Technol. 19 (6) (2010), 065005.

[55] J. Jansky, P. Le Delliou, F. Tholin, Z. Bonaventura, P. Tardiveau, A. Bourdon, S. Pasquiers, Propagation of an air discharge at atmospheric pressure in a capillary glass tube: influence of the tube radius on the discharge structure, IEEE Trans. Plasma Sci. 39 (11) (2011) 2106–2107.

[56] J. Jánský, A. Bourdon, Simulation of helium discharge ignition and dynamics in thin tubes at atmospheric pressure, Appl. Phys. Lett. 99 (16) (2011), 161504.

[57] E. Robert, E. Barbosa, S. Dozias, M. Vandamme, C. Cachoncinlle, R. Viladrosa, J. M. Pouvesle, Experimental study of a compact nanosecond plasma gun, Plasma Process. Polym. 6 (12) (2009) 795–802.

[58] Y. Akishev, M. Grushin, V. Karalnik, A. Monich, A. Petryakov, N. Trushkin, Self-pulsing regime of dc electric discharge in dielectric tube filled with water containing gas bubble, IEEE Trans. Plasma Sci. 36 (4) (2008) 1142–1143.

[59] S. Schröter, R. Pothiraja, P. Awakowicz, N. Bibinov, M. Böke, B. Niermann, J. Winter, Time-resolved characterization of a filamentary argon discharge at atmospheric pressure in a capillary using emission and absorption spectroscopy, J. Phys. D. Appl. Phys. 46 (46) (2013), 464009.

[60] M. Olde Riekerink, M. Claase, G. Engbers, D. Grijpma, J. Feijen, Gas plasma etching of Peo/Pbt segmented block copolymer films, J. Biomed. Mater. Res. A 65 (4) (2003) 417–428.

[61] N. De Geyter, R. Morent, T. Desmet, M. Trentesaux, L. Gengembre, P. Dubruel, C. Leys, E. Payen, Plasma modification of polylactic acid in a medium pressure dbd, Surf. Coat. Technol. 204 (20) (2010) 3272–3279.

[62] Y.N. Shin, B.S. Kim, H.H. Ahn, J.H. Lee, K.S. Kim, J.Y. Lee, M.S. Kim, G. Khang, H. B. Lee, Adhesion comparison of human bone marrow stem cells on a gradient wettable surface prepared by Corona treatment, Appl. Surf. Sci. 255 (2) (2008) 293–296.

[63] G. Aziz, R. Ghobeira, R. Morent, N. De Geyter, Plasma polymerization for tissue engineering purposes, Recent Res. Polymerization (2018) 69.

[64] A. Nandakumar, Z.T. Birgani, D. Santos, A. Mentink, N. Auffermann, K. van der Werf, M. Bennink, L. Moroni, C. van Blitterswijk, P. Habibovic, Surface modification of electrospun fibre meshes by oxygen plasma for bone regeneration, Biofabrication 5 (1) (2012), 015006.

[65] N. De Geyter, R. Morent, C. Leys, L. Gengembre, E. Payen, Treatment of polymer films with a dielectric barrier discharge in air, helium and argon at medium pressure, Surf. Coat. Technol. 201 (16) (2007) 7066–7075.

[66] M.P. Prabhakaran, J. Venugopal, C.K. Chan, S. Ramakrishna, Surface modified electrospun nanofibrous scaffolds for nerve tissue engineering, Nanotechnology 19 (45) (2008), 455102.

[67] S. Pineda-Castillo, A. Bernal-Ballén, C. Bernal-López, H. Segura-Puello, D. Nieto-Mosquera, A. Villamil-Ballesteros, D. Muñoz-Forero, L. Munster, Synthesis and characterization of poly (Vinyl Alcohol)-chitosan-hydroxyapatite scaffolds: a promising alternative for bone tissue regeneration, Molecules 23 (10) (2018) 2414.

[68] S.W. Kim, H.K. Bae, H.S. Nam, D.J. Chung, P.H. Choung, Peripheral berve regeneration through nerve conduit composed of alginate-collagen-chitosan, Macromol. Res. 14 (1) (2006) 94–100.

[69] K. Arcaute, B.K. Mann, R.B. Wicker, Fabrication of off-the-shelf multilumen poly (Ethylene Glycol) nerve guidance conduits using stereolithography, Tissue Eng. Part C Methods 17 (1) (2011) 27–38.

[70] G.C. De Ruiter, I.A. Onyeneho, E.T. Liang, M.J. Moore, A.M. Knight, M.J. Malessy, R.J. Spinner, L. Lu, B.L. Currier, M.J. Yaszemski, Methods for in vitro characterization of multichannel nerve tubes, J. Biomed. Mater. Res. A 84 (3) (2008) 643–651.

[71] L. Moroni, J. De Wijn, C. Van Blitterswijk, Three-dimensional fiber-deposited Peot/Pbt copolymer scaffolds for tissue engineering: influence of porosity, molecular network mesh size, and swelling in aqueous media on dynamic mechanical properties, J. Biomed. Mater. Res. A 75 (4) (2005) 957–965.

[72] C. Masciullo, R. Dell'Anna, I. Tonazzini, R. Böettger, G. Pepponi, M. Cecchini, Hierarchical thermoplastic rippled nanostructures regulate schwann cell adhesion, morphology and spatial organization, Nanoscale 9 (39) (2017) 14861–14874.

[73] V. Brunetti, G. Maiorano, L. Rizzello, B. Sorce, S. Sabella, R. Cingolani, P. Pompa, Neurons sense nanoscale roughness with nanometer sensitivity, Proc. Natl. Acad. Sci. 107 (14) (2010) 6264–6269.

[74] W. Liu, J.C. Zhan, Y. Su, T. Wu, C.C. Wu, S. Ramakrishna, X.M. Mo, S.S. Al-Deyab, M. El-Newehy, Effects of plasma treatment to nanofibers on initial cell adhesion and cell morphology, Colloids Surf. B Biointerfaces 113 (2014) 101–106.

[75] A.M. Pappa, V. Karagkiozaki, S. Krol, S. Kassavetis, D. Konstantinou, C. Pitsalidis, L. Tzounis, N. Pliatsikas, S. Logothetidis, Oxygen-plasma-modified biomimetic nanofibrous scaffolds for enhanced compatibility of cardiovascular implants, Beilstein J. Nanotechnol. 6 (2015) 254–262.

[76] J. Wu, Z. Mao, H. Tan, L. Han, T. Ren, C. Gao, Gradient biomaterials and their influences on cell migration, Interface Focus 2 (3) (2012) 337–355.

[77] E.W. Chan, M.N. Yousaf, A photo-electroactive surface strategy for immobilizing ligands in patterns and gradients for studies of cell polarization, Mol. BioSyst. 4 (7) (2008) 746–753.

[78] V.C. Hirschfeld-Warneken, M. Arnold, A. Cavalcanti-Adam, M. López-García, H. Kessler, J.P. Spatz, Cell adhesion and polarisation on molecularly defined spacing gradient surfaces of cyclic rgdfk peptide patches, Eur. J. Cell Biol. 87 (8–9) (2008) 743–750.

[79] M. Arnold, V.C. Hirschfeld-Warneken, T. Lohmüller, P. Heil, J. Blümmel, E. A. Cavalcanti-Adam, M. López-García, P. Walther, H. Kessler, B. Geiger, Induction of cell polarization and migration by a gradient of nanoscale variations in adhesive ligand spacing, Nano Lett. 8 (7) (2008) 2063–2069.

[80] A. Cooper, N. Bhattarai, M. Zhang, Fabrication and cellular compatibility of aligned chitosan-pcl fibers for nerve tissue regeneration, Carbohydr. Polym. 85 (1) (2011) 149–156.

[81] N. Abbasi, S. Soudi, N. Hayati-Roodbari, M. Dodel, M. Soleimani, The effects of plasma treated electrospun nanofibrous poly (Epsilon-Caprolactone) scaffolds with different orientations on mouse embryonic stem cell proliferation, Cell J. 16 (3) (2014) 245–254.

[82] N. Recek, M. Resnik, H. Motaln, T. Lah-Turnsek, R. Augustine, N. Kalarikkal, S. Thomas, M. Mozetic, Cell adhesion on polycaprolactone modified by plasma treatment, Int. J. Polym. Sci. 2016 (2016) 1–9.

[83] D.-H. Kim, P.P. Provenzano, C.L. Smith, A. Levchenko, Matrix nanotopography as a regulator of cell function, J. Cell Biol. 197 (3) (2012) 351–360.

[84] W. Wang, S. Itoh, K. Konno, T. Kikkawa, S. Ichinose, K. Sakai, T. Ohkuma, K. Watabe, Effects of Schwann cell alignment along the oriented electrospun chitosan nanofibers on nerve regeneration, J. Biomed. Mater. Res. A 91 (4) (2009) 994–1005.